9

Sediment Production, Evolution and Provenance

9.1 The Formation of Sediment

There is a complex web of processes affecting the generation of sediment from bedrock weathering, through transport and intermittent storage, to eventual long-term deposition in a sedimentary sink. This web of processes imparts a certain textural and compositional imprint on the final deposit, yet joined-up approaches to the pathway from source to sink are rare (Ibbeken and Schleyer, 1991). Gert Jan Weltje wrote in Weltje (2012) (p.4):

> Current approaches to modelling of surface processes treat the coupled evolution of source areas and sedimentary basins in terms of bulk mass transfer only, and do not take into account compositional and textural sediment properties.

In such mass balance approaches, the generation of sediment in source regions is commonly treated as a boundary condition for sediment supply, rather than as a dynamic system in its own right. Consequently, the properties of weathering products, both texturally and compositionally, entering the sediment cascade remain poorly constrained. Rare examples of where a mass balance approach is integrated with a provenance study are taken from modern and Quaternary environments (for example, Weltje and Brommer (2011)) rather than from ancient sediment routing systems. The advantage of integrating sediment generation with Earth surface process models is that the properties of sediment entering the transport network of sediment routing systems can be predicted and parameterised under different conditions of climate and tectonics, instead of being simply treated as a volumetric or solid mass boundary condition.

The evolution of sediment involves important modifications to the original parent rock (Johnsson, 1993). Such modifications might be chemical and mechanical weathering of bedrock and regolith, or the fractionation of grains during transport. Compositional variation within a sediment routing system is due to (1) mixing of grains from different sources and (2) chemical and mechanical weathering of the grain population, which may take place during regolith formation at source, or during transport and storage en route to a depositional sink (Weltje, 2012).

Figure 9.1 illustrates a simple mixing model of a fault-bounded sedimentary basin with two catchments feeding sediment to an adjacent basin. There is a lateral variation in

https://doi.org/10.1017/9781316135754.010 Published online by Cambridge University Press

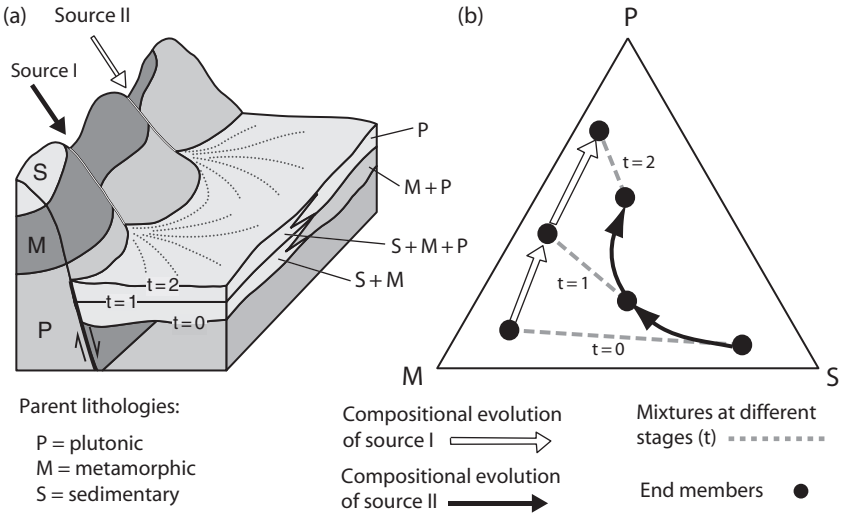

Figure 9.1 Lateral and vertical variation of sediment composition in a fault-bounded basin fed by two catchments. (a) Uplift of lithologically heterogeneous source areas results in progressive unroofing of bedrocks; (b) Compositional evolution of the sources and the range of mixtures in the basin-fill at three points in time ($t1$ to $t3$) are shown in the ternary diagram. Modified from Weltje (2012)(fig.3) with permission from Elsevier.

composition caused by the differences in the lithologies being eroded in the two source catchments and dispersed into the basin, and a vertical variation caused by progressive unroofing over time of rocks in the source catchments. Conglomerate clast compositions can be used to investigate the progressive erosion of lithologically distinct units in the source catchments (Graham et al., 1986; Steidtmann and Schmitt, 1988; Pivnik, 1990). Sediment compositions can therefore potentially be used to estimate the proportional contributions of different sediment sources to rivers or other agents of sediment transport such as the wind. The proportional contributions can be converted to absolute rates of sediment flux by using independent estimates of the total sediment discharge, for example, from measured sediment loads of rivers (Vezzoli et al., 2004; Vezzoli, 2004).

Different source area lithologies have a range of capacities for generating sediment by weathering and erosion, and different bedrock types have different capacities for breaking down into particular grain-size ranges. The Sand Generation Index (SGI), for example, quantifies the relative efficiency of sand production from different lithologies (Palomares and Arribas, 1993; Arribas and Tortosa, 2003). The SGI is a variable that reflects the relative sand-generating capability of a certain bedrock when compared to another bedrock type that is generating sand-grade sediment under the same topographic and climatic conditions. The SGI of a given bedrock type A of a dual source A+B, denoted $SGI_{A(A+B)}$, is expressed in terms of the outcrop area of bedrock type A, denoted S_A, needed to produce a sand composed of equal amounts of both A and B bedrocks:

https://doi.org/10.1017/9781316135754.010 Published online by Cambridge University Press

$$\mathrm{SGI}_{A(A+B)} = [S_A + S_B]/S_A \tag{9.1}$$

where $[S_A + S_B]$ is the total surface area of the source region (100%), and S_A and S_B are the outcrop areas of bedrocks A and B within the source region required to produce sand with the average modal composition observed. Likewise, the SGI for bedrock type B is

$$\mathrm{SGI}_{B(A+B)} = [S_A + S_B]/S_B \tag{9.2}$$

Each rock type has a different potential to generate sand, depending on properties such as its mineralogy, average crystal size and microfabric (cleavage, fractures) (Palomares and Arribas, 1993). Studies of metamorphic and granitic terrains show that the SGI of granitoid rocks is 14–20 times the SGI of slates and schists, and the SGI of gneisses is five times that of slates and schists. In sedimentary terrains, siliciclastic sources are the most productive sedimentary source of sand in the fine, medium and coarse fractions of river sands analysed by Arribas and Tortosa (2003) from catchments in the Iberian Range, Spain (Table 9.1) (Figure 9.2). The SGI of siliciclastic sources varies from 20–4, whereas the SGI of carbonates varies from 1.0–1.3. Siliciclastic sources are therefore 3–20 times more efficient at producing medium sand-grade sediment than carbonates.

Vezzoli et al. (2004) modified the original concept of the Sand Generation Index in order to assess the relative contributions of seven end-member sources of detritus in the Dora Baltea Basin, Western Alps (Table 9.2). The seven bedrock types are shown in ternary diagrams of light fraction and heavy fraction (Figure 9.3). The Monte Bianco Massif has the highest SGI index in the Dora Baltea Basin (SGI of 16.4), followed by the Austroalpine

Table 9.1 *Sand Generation Index (SGI) values from compound sedimentary source areas calculated from the medium sand fraction of river deposits in the Iberian Range. From Arribas and Tortosa (2003)(tab.3, p.289), with permission of Elsevier.*

Compound sedimentary source	Surface area corresponding to average composition[a] (%)	SGI
Siliciclastics+carbonates		
Siliciclastics	5–5	20–4
Carbonates	95–75	1.0–1.3
Dolostones+limestones		
Limestones	18–30	5.5–3.3
Dolostones	82–70	1.2–1.4
Carbonate lithofacies		
Micritic limestones	35–45	2.8–2.2
Micritic dolostones	(100)[b]	(1)
Sparitic limestones	5–35	20–2.8
Sparitic dolostones	40–75	2.5–1.3

[a] Percentages estimated visually from diagrams such as Figure 9.2.

[b] In parentheses: unequivocal assignment of grain type to source lithology in the case of dolomicrite.

https://doi.org/10.1017/9781316135754.010 Published online by Cambridge University Press

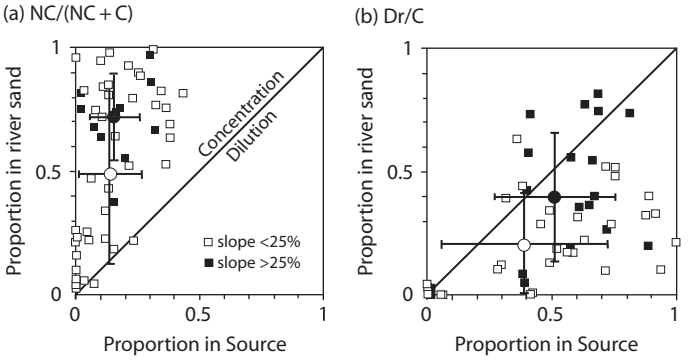

Figure 9.2 Plots of two petrographic indices versus indices of the surface exposure of lithologies in the source region for the medium sand fraction of low-order stream deposits from the Iberian Range, Spain. (a) NC, Non-carbonate (siliciclastic) rocks; C, Carbonate rocks. (b) Dr, sparitic dolostones. Means with standard deviation of each group of samples is shown. Samples are grouped according to slope. Dilution is the case where the petrographic ratio is lower in river sands than in surface area of exposure of lithologies, as in (b), showing that sparitic dolostones are under-represented in medium sand fractions. Concentration occurs where the petrographic ratio is higher in river sands, as in (a), showing that siliciclastic rocks are a highly productive source of sand. After Arribas and Tortosa (2003) (fig.9) with permission of Elsevier.

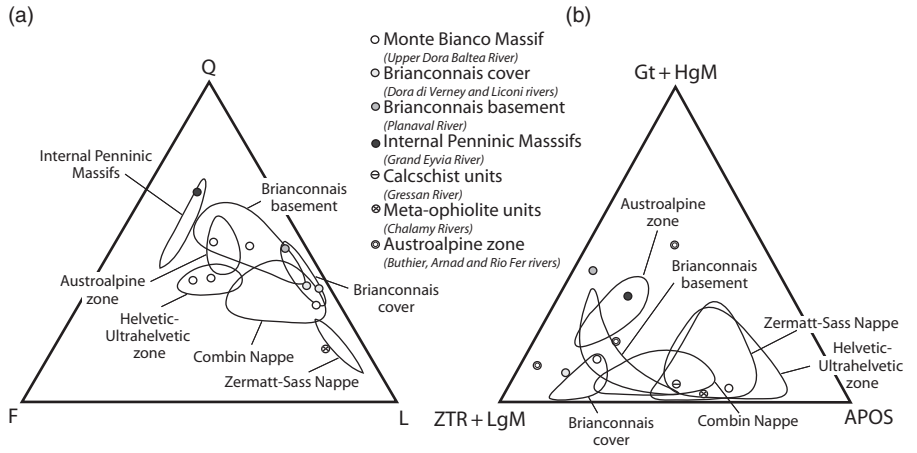

Figure 9.3 (a) Framework composition (Quartz-Feldspar-Lithics) of detritus from the end-member sources of the Dora Baltea basin compared to statistically rigorous confidence regions about the mean compositions of (mainly) Alpine domains. (b) Mineralogical signatures, with vertices representing Gt+HgM (garnet and high-grade metamorphic minerals), ZTR+LgM (ultrastables and low-grade metamorphic minerals), and APOS (amphiboles, pyroxenes, olivine and spinel). Modified from Vezzoli et al. (2004) (figs.3, 4) with permission of Elsevier.

domain (SGI of 1.4). The high capacity for the production of sand-grade sediment of the Monte Bianco Massif, despite occupying just 3% of the whole catchment, is promoted by its granitoid lithology, heavy glaciation and extreme relief - it is the highest peak in Europe at 4,810 m.a.s.l.

https://doi.org/10.1017/9781316135754.010 Published online by Cambridge University Press

Table 9.2 *Contribution from various tectonic units to the bed load of rivers in the Dora Baltea Basin. From Vezzoli et al. (2004) (tab.6, p.243) with permission of Elsevier.*

Tectonic unit	Contribution based on bulk composition (%)	Contribution based on Sand Generation Index
Monte Bianco Massif	50 (2)	16.4
Briançonnais cover	1 (1)	0.1
Briançonnais basement	2 (1)	0.1
Penninic massifs	7 (2)	1
Calcschist units	1 (1)	0.1
Meta-ophiolite units	4 (2)	0.2
Austroalpine zone	35 (3)	1.4

Percentages based on bulk composition were averaged from several independent trials. Numbers in parentheses are 1σ standard deviation. Meta-ophiolites refers to Zermatt-Sass Nappe.

The total sediment flux of the Dora Baltea Basin is 1 Mt yr^{-1}, comprising 0.59 Mt yr^{-1} of bedload and 0.41 Mt yr^{-1} of suspended load. Analyses of sediment composition indicate that greater than 75% of the Dora Baltea bedload is derived from tributaries with sources in the highest granitoid peaks above 4,000 m.a.s.l., though these tributaries drain only 36% of the total catchment area (Vezzoli, 2004). The Monte Bianco Massif alone produces 0.294 ± 0.006 Mt of arkosic sands per year, representing 50% of the total bedload flux of the Dora Baltea Basin. Based on the total sediment flux and drainage basin area, the sediment yield for the entire Dora Baltea catchment is 306 t km^2 yr^{-1} and the equivalent denudation rate is 0.12 mm yr^{-1}.

Di Giulio et al. (2003) also analysed the composition of river bed sands in relation to the surface exposure of sedimentary (and minor metamorphic) lithologies in small catchments in the northern Apennines. Siliciclastic rocks in source areas are under-represented (diluted) in river sands compared to their outcropping surface area. Carbonate rocks are also under-represented. Some rock types, such as metamorphic rocks, occur in quantities of up to 20% of sand samples despite the fact that they are absent in the source area catchments, indicating that grains are *recycled* from older siliciclastic rocks (Zuffa, 1987). When the expected amount of siliciclastic rocks in the drainage area is recalculated to account for recycling of grains from older coarse-grained siliciclastic rocks, siliciclastic rocks re-plot as slightly over-represented in river sands, as anticipated from other studies (Arribas and Tortosa, 2003).

There is therefore a difference between the bulk composition of a parent rock and the composition of the grain assemblage in regolith or bedload of upland rivers. This difference increases over time as the sediment is dispersed through the sediment routing system (Weltje, Meijer, and de Boer, 1998).

The primary controls on the type of sediment released into the sediment cascade are the mineralogical composition, texture and crystal or particle size of the parent rocks.

https://doi.org/10.1017/9781316135754.010 Published online by Cambridge University Press

The parent rocks are transformed into sediment by weathering, the extent of which depends on weathering rate and the residence time of material in the weathering environment. The rate of silicate weathering is fundamentally controlled by climate, specifically temperature and precipitation (White and Brantley, 1995). Tectonics provides relief, which controls the residence time for weathering by the onset of creep or mass flow of hillslope material downslope. The extent of chemical weathering can be monitored through the ratio of the abundance of quartz (Q) to feldspars (F). Preferential weathering of feldspars by acid hydrolysis causes an increase in $\log(Q/F)$ over time.

Weltje (1994) generalised the cumulative chemical weathering index of Grantham and Velbel (1988) to obtain a semi-quantitative index of the extent of weathering under different climatic and physiographic conditions. The distance in compositional space relative to the composition of parent rocks (w) is the integration of the rate of weathering V over the amount of time elapsed since weathering began t:

$$w = \int V \mathrm{d}t = \bar{V}t \tag{9.3}$$

where $\bar{V}$ is the time-averaged weathering rate. The weathering index of Weltje (1994) (I_w) relates w to present-day climate and physiography of sediment sources:

$$I_w = CR \simeq w \tag{9.4}$$

where C is a semi-quantitative indicator of climate (essentially rainfall) and R is a semi-quantitative indicator of relief. C is used as a proxy for time-averaged weathering rate and R is assumed to be inversely proportional to residence time in the source area. The weathering index I_w takes integer values between 0 and 4 in Weltje (1994) and Weltje et al. (1998), since S and R are both integers (with values of 0, 1 and 2) as shown in Table 9.3.

The weathering rate can also be expressed in the form of an exponential relationship

$$V = RSI\left(\frac{c_1 Q_i \exp(c_2/(c_3 T_a))}{H_{reg}}\right) \tag{9.5}$$

where RSI is a regolith supply index, with values of $0 - 1$, where a value of 1 indicates the availability of unlimited regolith for the ambient erosion rate, T_a is the year-average catchment temperature in °C, Q_i is the soil infiltration rate in mm yr^{-1}, H_{reg} is the regolith thickness in mm, and c_1 to c_3 are constants (Forzoni et al., 2014).

The extent of weathering of parent rock to produce sediment can be assessed by using the log ratios of principal framework elements. Examples are $\log(Q/F)$ and $\log(Q/R)$, where Q is quartz content, F is feldspar content and R is the rock fragment content of the sand. Simultaneous use of both logratios discriminates the parentage and weathering history of a sand. The values of both logratios correlate with I_w because quartz is more resistant to weathering than feldspar and rock fragments. The general trend of compositional evolution with increasing values of the weathering index is therefore towards high values of both $\log(Q/F)$ and $\log(Q/R)$ (Figure 9.4).

https://doi.org/10.1017/9781316135754.010 Published online by Cambridge University Press

Table 9.3 *Integer values of climate (rainfall) parameter C, relief R and weathering index $I_w = CR$. After Weltje et al. (1998)(tab.1, p.134) with permission of John Wiley & Sons Inc.*

C	Climate
0	(Semi) arid and Mediterranean
1	Subhumid
2	Humid
R	Relief
0	High (mountains)
1	Moderate (hills)
2	Low (plains)
I_w	Weathering index
0	Unweathered
1	Slightly weathered
2	Moderately weathered
4	Intensely weathered

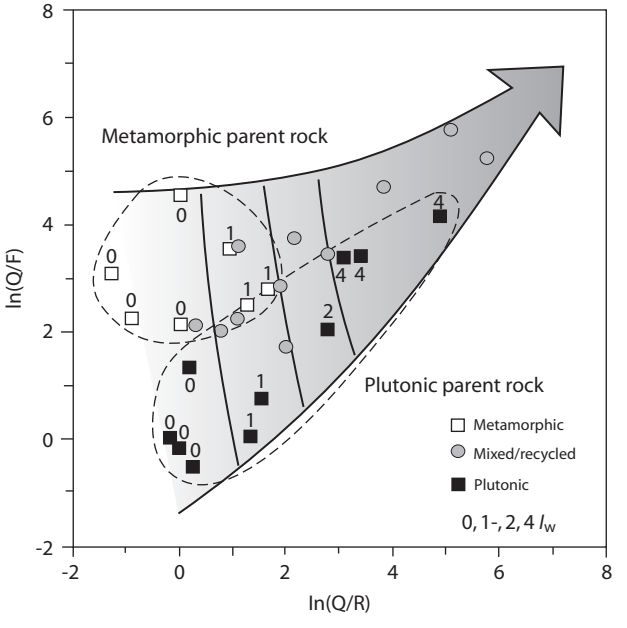

Figure 9.4 Plot of logratios for medium grained river sands, showing relationship between petrographic composition, parent rock type and weathering index I_w (proxy for climatic and physiographic conditions in catchment source areas *CR*) for two clusters of first-cycle sands derived from monolithologic catchments. Mixed/recycled samples are from Orinoco drainage basin. Modified from Weltje (1994) and Weltje et al. (1998) (fig.4) with permission of John Wiley & Sons Inc.

https://doi.org/10.1017/9781316135754.010 Published online by Cambridge University Press

Changes in the rate of sediment supply can be detected in shifts in sediment grain size and composition, both of which are related to weathering history. Since weathering rates in humid-tropical conditions are fast ($\sim 10^4$ yr timescale) (Johnsson and Meade, 1990), and similar rates are found in other climatic zones (Nesbit, Fedo, and Young, 1997), high frequency variations in sediment supply are potentially attributable to changes in the extent of weathering, driven, for example, by Milankovitch-band climate change (Section 10.2). Variations in $\log(SiO_2/Al_2O_3)$ in Pliocene turbidites in Corfu (Greece) show that the extent of weathering decreases from the base to the top of each depositional lobe, indicating that weathering of sands in the subaerial part of the sediment routing system took place prior to lobe reactivation (Weltje and de Boer, 1993).

A combination of grain size and compositional characteristics in the non-biogenic portion of deep sea sediments makes it potentially possible to infer palaeoclimate in the source areas for sediment (Weltje and Prins, 2003). The grain-size distribution of a sediment sample represents a mixture of sediment populations corresponding to the different mechanisms of sediment production and sediment transport. The grain-size characteristics of a finite number of so-called dynamic populations represent a certain set of processes of sediment production and transport. Each dynamic population can be tied to a specific source and dispersal mechanism. The bulk composition or mineralogy of a sample is usually a function of the grain-size distribution, since each size fraction has a characteristic fingerprint in terms of composition. Dynamic populations are expected to be markedly different, for example, in turbidites, where transport and deposition are highly size-selective, and ice-rafted detritus, where processes of sediment production may dominate over processes of transport. Examples of palaeoclimate interpretations based on the recognition of dynamic populations in marine sediment are found in Weltje and Prins (2003).

9.2 Precipitation, Vegetation and Erosion

Climate, expressed in terms of mean annual precipitation, precipitation variability, vegetation cover, temperature or other climate-related indices, is a major control on the supply of sediment to sedimentary basins (Hooke, 2000). Climatic influences are commonly expressed in terms of precipitation or effective precipitation, as in the seminal study of Langbein and Schumm (1958). The effective precipitation is the annual rainfall that would be required, on average, to produce the observed run-off. The Langbein–Schumm curve of effective precipitation versus sediment yield shows a maximum in yield at $\sim$300 mm yr^{-1} after which sediment yield decreases with increasing precipitation (Figure 9.5), which is thought to be due to the binding effect of vegetation at high values of precipitation. The curve presented by Dendy and Bolton (1976) has a similar shape, but with the yield maximum at $\sim$500 mm yr^{-1}, whereas the curve of Douglas (1967) is more complex, with a peak in yield at $\sim$450 mm yr^{-1} but with an increasing trend in yield at high levels of precipitation (Figure 9.5). Wilson (1973) reported similar results. The difficulty in interpreting the plots of effective precipitation and sediment yield is the possible impact of other factors such as relief, drainage basin size and bedrock lithology.

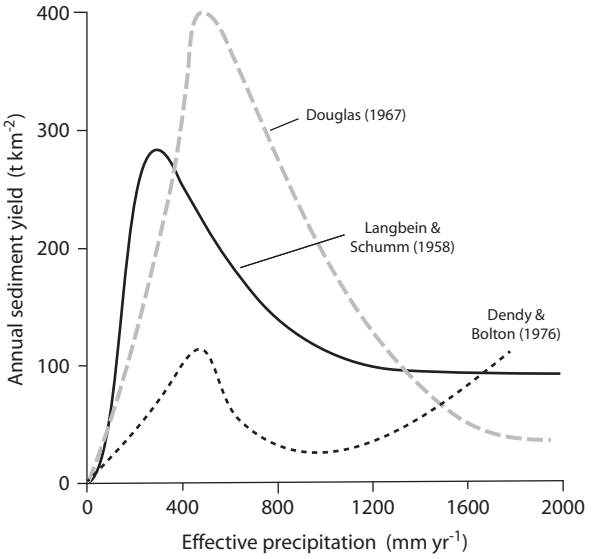

Figure 9.5 Relationships between denudation rate measured as sediment yield and effective precipitation, for three authors. After Hooke (2000)(fig.2) with permission of Geological Society of America.

Precipitation varies seasonally and on shorter timescales, which contributes to the intensity of precipitation and the erosivity of run-off. Rainfall variability can be modelled using the relation p^2/P, where p is the maximum mean monthly precipitation and P is the mean annual precipitation (Fournier, 1960). Alternatively, the storm run-off rate P_s can be related to the mean annual run-off rate $\bar{P}$ by a 'total flood duration ratio' ζ, defined as the total fraction of a given year that the drainage basin is subject to flooding (Tucker and Slingerland, 1997). For example, if rainfall fell continually at a uniform rate throughout the year, ζ would be equal to 1. If it fell on one day only, ζ would be equal to 1/365. The instantaneous storm run-off rate is then

$$P_s = \frac{\bar{P}}{\zeta} \tag{9.6}$$

Tucker and Slingerland (1997) varied $\bar{P}$, P_s and ζ in model runs using a landscape evolution model. Catchments responded strongly to run-off intensity, as opposed to mean precipitation, increasing in denudation rate and sediment efflux with increasing rainfall intensity. However, some authors have found no significant correlation between rainfall variability and sediment yield in global data sets (Summerfield and Hulton, 1994; Hovius, 1998). The effects of variability are most likely at their strongest in semi-arid and arid regimes. Precipitation variability may be more important than mean precipitation in long-term landscape evolution (Tucker and Bras, 2000), but the effect of short-term rainfall variability on long-term landscape development is likely to be smaller than the impact of human activities (Baartman et al., 2013).

The distribution of storm (or daily) rainfalls is commonly expressed as an exponential function, in which the number density of days with rainfall greater than r is estimated as

$$N(r) = N_0 \exp(-r/r_0) \tag{9.7}$$

where N_0 is the number of days on which rain fell, and r_0 is the mean rain per rain day, so $r_0 N_0$ is the total annual rainfall R. Erosion of soil and regolith requires overland flow, which can only be generated above a certain storm size with a run-off threshold, which is a storage capacity of the soil or regolith h. In a single storm the overland flow per unit area j is:

$$j = r - h \tag{9.8}$$

Summing equation (9.8) over all the rainfall events exceeding the run-off threshold gives

$$J = \int_h^\infty (r - h) N(r) \mathrm{d}r = N_0 r_0 \exp(-h/r_0) \tag{9.9}$$

Assuming sediment yield is proportional to the square of the water discharge, the yield from a single rainfall event y is

$$y \propto (r - h)^2 \tag{9.10}$$

which when summed over the frequency distribution gives the total sediment yield Y:

$$Y \propto \int_h^\infty (r - h)^2 N_0 \exp(-r/r_0) \mathrm{d}r = 2 N_0 r_0^2 \exp(-h/r_0) \tag{9.11}$$

which is known as the Cumulative Erosion Potential (CEP) (DePloey, Kirkby, and Ahnert, 1991). The CEP combines the effects of rainfall distribution through N_0 and r_0 and a soil hydraulic parameter h_0 to give a measure of the climatic component in soil erosion. As an example, if there are 100 rain-days per year (N_0), the mean rainfall per rain-day (r_0) is 10 mm, the annual rainfall (R) is 1000 mm. Letting the run-off threshold (h_0) be 30 mm, the CEP becomes ~1,000. If we reduce the number of rain-days to 50, but increase the mean rainfall per rain-day to 20 mm, which reflects a more seasonal regime, CEP doubles to ~2,000.

The CEP model has been extended to incorporate the effects of the growth of vegetation and the impact of biomass on soil strength. The CSEP (Cumulative Soil Erosion Potential) of Kirkby and Cox (1995) gives a global picture that shows highest erosion potential in monsoonal climates and lowest erosion potential in deserts and cool temperate belts.

Plots of CSEP versus annual rainfall show significant differences between non-seasonal and seasonal patterns of rainfall, and as a function of mean annual temperature (Figure 9.6). The overall form of the curves is similar to that proposed by Langbein and Schumm (1958), with maximum erosion rate in semi-arid climates, a minimum in temperate climates and a renewed rise at very high rainfalls. In seasonal Mediterranean-type climates, rainfall seasonality has opposite effects at high and low temperatures. At low temperatures, seasonality increases erosion potential, whereas at high temperatures, seasonality reduces erosion potential. Clearly, there is a limit to the applicability of the full CSEP model to ancient sediment routing systems where parameters describing the rainfall regime and the

https://doi.org/10.1017/9781316135754.010 Published online by Cambridge University Press

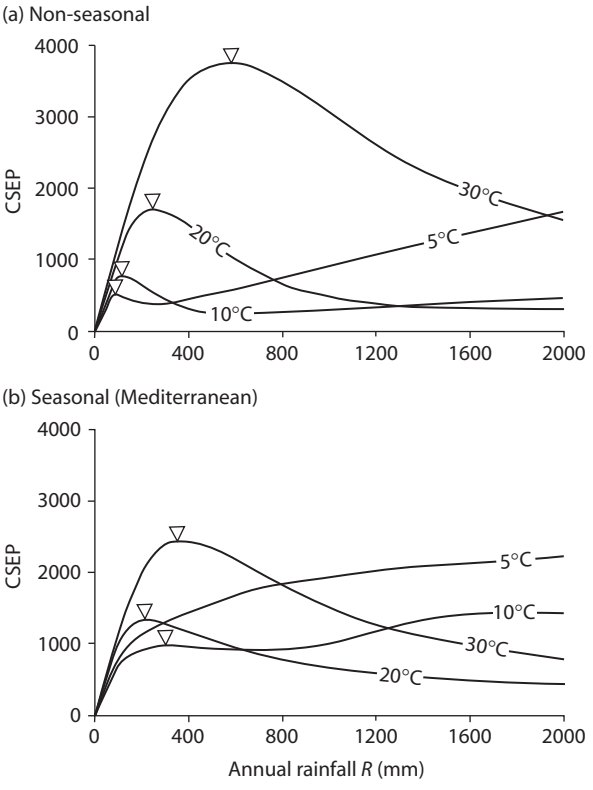

Figure 9.6 Estimated CSEP using equation (9.11). Triangles show erosion maxima. (a) CSEP for rainfall in non-seasonal climates (each month has the same amount of rainfall), with a strong semi-arid maximum and temperate zone minimum, particularly at high temperatures. (b) CSEP for rainfall with strong seasonality (wet winter, Mediterranean climate). The temperate zone minimum seen in (a) is reduced, except at high temperatures. After Kirkby and Cox (1995)(fig.6) with permission of Elsevier.

vegetation-organic growth dynamics are unknown. However, the curves in Figure 9.6 are a starting point for making educated guesses of the likely impact of climate change on erosion and sediment flux in the geological past, especially where the palaeoclimate can be well constrained (Van der Zwan, 2002). The CSEP model has been used to understand variations of sediment production linked to Quaternary glacial-interglacial cycles in the Great Basin, United States (Leeder et al., 1998).

A global scale view can be gained by implementing a soil erosion model developed from the results of plot-scale ($\sim$1 m^2 to 30 m^2) erosion experiments and has the form

$$E = kJ^2S^{1.67}\exp(-0.07v) \tag{9.12}$$

where E is erosion in mm day^{-1}, k is a soil erodibility constant with values betweeen 0.02 and 0.69, J is the overland flow in mm day^{-1}, S is the slope and v is the vegetation cover expressed as a percentage (Zhang, Drake, and Wainwright, 2002). Rates of overland flow

https://doi.org/10.1017/9781316135754.010 Published online by Cambridge University Press

can be expressed by a modification of the Carson and Kirkby (1972) model, assuming that daily rainfall amounts approximate an exponential frequency distribution within a time period and that the real soil water storage capacity is affected by the initial soil moisture:

$$J_i = P_i \exp(-(rc - Q_{Ti})/(P_i/N_i)) \tag{9.13}$$

where J_i is the overland flow (run-off) in the given time period (mm), N_i is the number of rain-days in the given time period, Q_{Ti} is the total initial soil moisture (mm), rc is the potential water storage capacity (mm) equal to 300 mm, representing a rooting zone, and i is the ith time period from 1 to 12 for monthly intervals (Zhang et al., 2002). If $k = 0.4$, $S = 0.05$, $v = 0.6$ and $J = 730$ mm yr^{-1}, the calculated erosion rate E is 0.06 mm yr^{-1}.

A soil erosion model of the form in equation (9.12) has been used at timescales appropriate for long-term landscape dynamics, where the erosion rate E is termed the maximum achievable erosion rate, applying to the case of unlimited regolith availability (Forzoni et al., 2014). Regolith production rates may be significantly lower than the potential erosion rate (Tucker and Slingerland, 1997). Forzoni et al. (2014) therefore introduced a regolith supply index *RSI* with values of 0 to 1 in order to simulate both detachment-limited and transport-limited conditions.

Regolith production rates can be approximated by the rate of conversion of bedrock to regolith by physical and chemical weathering. This conversion rate is commonly taken as inversely proportional to the thickness of regolith cover C (Tucker and Slingerland, 1997):

$$\omega = k_w \exp(-C/C^*) \tag{9.14}$$

where ω is the vertical rate of descent of a weathering front, k_w is the weathering descent rate for bare bedrock (that is, at $C = 0$), and C^* describes the rate at which the weathering rate decays with increasing regolith thickness. The bare bedrock regolith production rate k_w and the weathering decay constant C^* were given values of 0.0005 m yr^{-1} and 0.5 m respectively by Tucker and Slingerland (1997).

Annual precipitation varies with latitude (Figure 9.7), so the trends of sediment yield versus effective precipitation in Figure 9.5 can be viewed as a latitudinal zonation. Precipitation values of greater than 1,000 mm yr^{-1} are mostly restricted to tropical latitudes, with the exception of wet temperate locations in the southern hemisphere such as New Zealand and southern Chile. Peaks in sediment yield, which occur at effective precipitation values of about 300–600 mm yr^{-1} are found principally in subtropical latitudes. Since rate of denudation is clearly mediated strongly by vegetation, changes in land vegetation over the Phanerozoic should modify the picture evident in Figure 9.5 (Schumm, 1968). Key developments were the advent of land vegetation (Late Silurian), the appearance of horsetails and ferns (Devonian), conifers (Carboniferous), flowering plants (end Jurassic) and the appearance of grasses near the end of the Cretaceous. Before the colonisation of the land surface by plants it is expected that there would be a simple linear trend of increasing sediment yield with increasing precipitation. If so, sediment routing systems in the Precambrian and the early Palaeozoic would have functioned considerably differently to those of today.

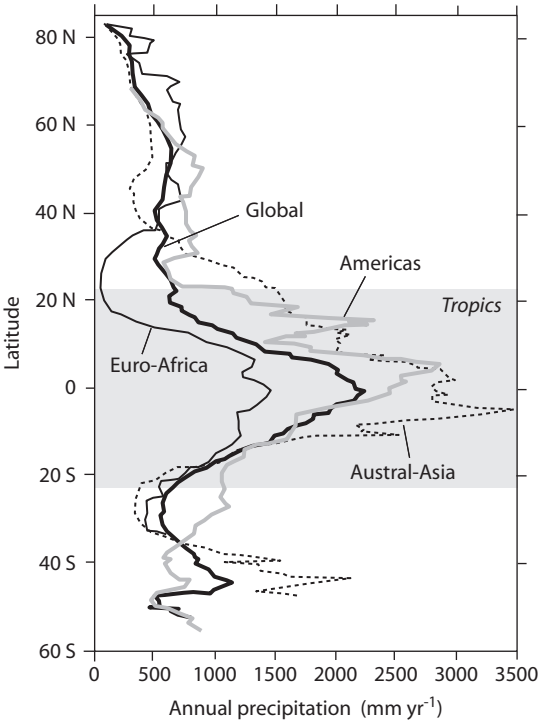

Figure 9.7 Latitudinal distribution of global precipitation and in the Americas, Euro-Africa and Austral-Asia. After Milliman and Farnsworth (2011)(fig.2.3) with permission of Cambridge University Press.

9.3 Grain-Size Mix of Sediment Supplied to Basins

A key factor in the downstream dispersal and fractionation of sediment is the grain-size distribution of sediment supplied by upstream catchments. Different distributions of grain size in the sediment supply to basins affect the pattern of downstream fractionation (Strong et al., 2005; Fedele and Paola, 2007; Duller et al., 2010; Whittaker et al., 2010; Armitage et al., 2011; Michael et al., 2013; Michael et al., 2014a; Schlunegger and Norton, 2015). Building an understanding of the impact of the changing distribution of grain size is vital for prediction of subsurface sedimentary architectures, gross depositional environments and sedimentary facies (Strong et al., 2005; Carvajal and Steel, 2012; Michael et al., 2013; Michael et al., 2014a) and forms a key element in the fields of sequence stratigraphy (Chapter 10) and basin analysis. It is important, therefore, to know the characteristics of and the controls on the grain-size mix serving as an initial condition for down-system dispersal (Allen et al., 2015b).

It is generally recognised that there is a paucity of information on the grain-size distributions of the weathering products that define the initial condition for sediment dispersal (Weltje, 2012). The crystal size distribution in crystalline parent rocks, for example,

https://doi.org/10.1017/9781316135754.010 Published online by Cambridge University Press

has been described as log-normal (Eberl, Drits, and Srodon, 1998), but it is not known whether this is a general rule for other rock types and in regolith comprising rock fragments and broken particles rather than individual mineralogical crystals. The size distribution of weathered crystalline rocks such as granites, which have undergone brittle disintegration, has also been found to be approximated by Rosin's (exponential) law (Krumbein and Tisdel, 1940; McEwen, Fessenden, and Rogers, 1959). Crushed materials and those undergoing mechanical disintegration such as scree, regolith (including on moons and other planets), pyroclastic material and subglacial tills have also been described by the Rosin law (Kittleman, 1964; Ibbeken, 1983; Deb and Sen, 2013) and the closely related Weibull distribution. Other workers have argued that materials that have undergone comminution commonly have a fractal distribution of size (Hartmann, 1969; Turcotte, 1997; Smalley et al., 2005; Allen et al., 2015b).

The formation of sediment from parent rocks is part of a general process of 'fragmentation' (Hartmann, 1969; Turcotte, 1997; Smalley et al., 2005). The most important process of fragmentation in the present context is the breakdown of parent rocks by the processes of weathering (Wu, Borkovee, and Sticher, 1993; Bitelli, Campbell, and Flury, 1999; Wells, Willgoose, and Hancock, 2008). Weathering is an example of fragment size reduction, resulting in soils, sediment and regolith containing fine-grained particles (Jefferson et al., 1997). This process of fragment size reduction, or comminution, is well known to result in fractal distributions of grain size (Hyslip and Vallejo, 1997) (Figure 9.8).

If the grain-size distribution of the sediment released into the cascade from source to sink (Burt and Allison, 2010) is to be modelled in a geomorphic context, it is necessary to

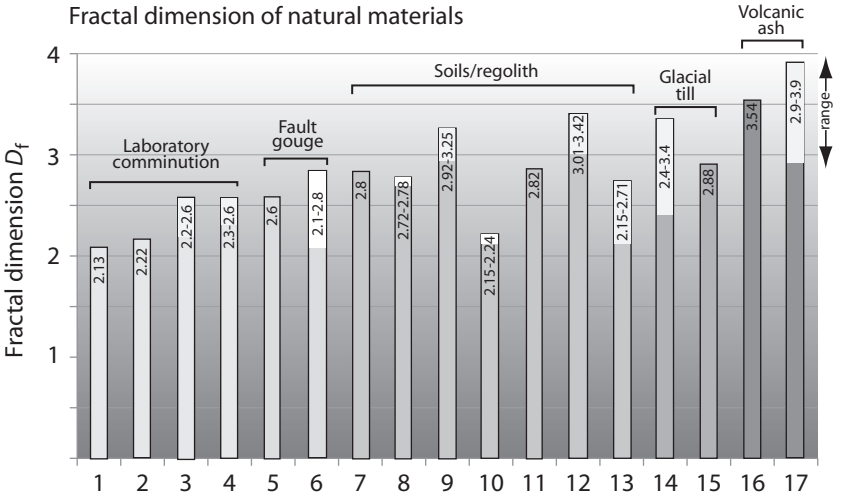

Figure 9.8 Average fractal dimension for a range of natural materials (rocks, soils, regolith, sediments). 1, disaggregated gneiss; 2, disaggregated granite; 3, 4, laboratory comminution of sand; 5, fault gouge; 6, cataclastic zone; 7, soils (general); 8, 52 gravelly and sandy soils; 9, semi-arid soils; 10, temperate soils; 11, loamy soils; 12, loess (quartz silt); 13, terrace sands and gravels; 14, 69 glacial tills; 15, glacial till; 16, volcanic ash and pumice; 17, 62 ash fall and ash flow deposits. From Allen et al. (2015b) (fig.1) with permission of University of Chicago Press.

https://doi.org/10.1017/9781316135754.010 Published online by Cambridge University Press

account for the combined effects of parent rock lithology and microstructure, topography, climate and the passage of time on the fragmentation process. However, in the context of geological sediment routing systems, the range of controls on the particle size distribution of sediment exported to sedimentary basins needs to be reduced to as few parameters as possible so that the method can be used where little is known about the contributing catchment areas, including their location, size, morphometry, climate and lithological make-up (Sømme et al., 2009).

If a parent rock breaks into smaller pieces, which themselves break into smaller pieces, and so on, we should expect the number of fragments N with a size greater than a certain linear dimension x to decrease as the linear dimension increases. The number of fragments with a linear dimension greater than x can be expressed by the fractal number relation

$$N(X > x) = Cx^{-D_f} \tag{9.15}$$

where D_f is the fractal dimension associated with fragmentation and C is a coefficient. D_f is typically between 2 and 4 for a range of fragment types over 4 to 5 orders of magnitude of x (Figure 9.8). The number of fragments can be substituted by the volume or mass of sediment with particle sizes greater than a certain linear dimension to enable comparison with empirical plots of grain-size distribution derived from sieving (Tyler and Wheatcraft, 1992; Hyslip and Vallejo, 1997). In such a case, equation (9.15) is modified from its number-specific form to a weight-specific form:

$$P(X < x) = \frac{M(X > x)}{M_T} = \left(\frac{x}{x_{max}}\right)^m \tag{9.16}$$

where P is the proportion by weight of particles smaller than the sieve size x, M is the weight (or mass) smaller than the sieve size, M_T is the total weight of sediment sieved, x_{max} is the maximum sieve or screen size (through which all particles pass), and m is an index of the spread of the particle size distribution given by the slope of the power law represented by equation (9.15). Since particle volume or weight is related to the cube of particle number (Turcotte, 1997), the parameter m is related to the fractal dimension by

$$D_f = 3 - m \tag{9.17}$$

Using equation 9.15, it can be seen that when the grain-size distribution is heavily loaded with fine particles the fractal dimension is large, and when the grain-size distribution is loaded with coarse particles the fractal dimension is small.

It can reasonably be expected that the grain-size distributions of sediment released from catchments will be similar to those of crushed or mechanically disintegrated materials rather than to sediments that have undergone profound reworking and sorting during transport. Hydraulic sorting during transport is thought to generate grain-size distributions of exponential or log-normal types (Section 9.4.2) (McEwen et al., 1959; Middleton, 1976; Ibbeken, 1983; Allen et al., 2015b). A number of different regolith and sediment types have therefore been analysed that might approximate the time-averaged characteristics of the sediment efflux of upland catchments on geological timescales. These materials include (1)

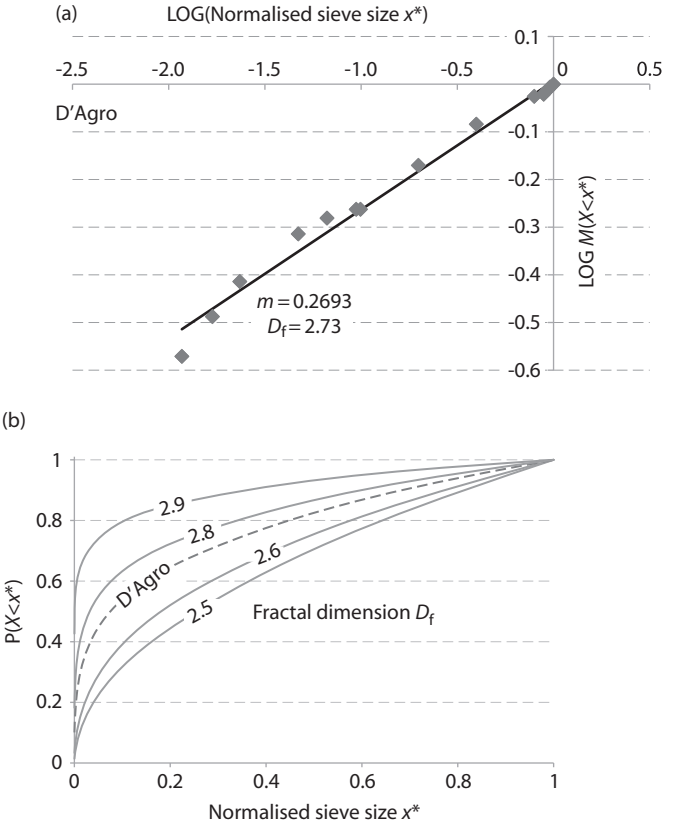

Figure 9.9 (a) Log-log plot of the normalised grain size $x^* = x/x_{max}$ versus the mass smaller than the sieve size with a straight line fit of gradient m. Data are for a sieved sample taken at a locality at the mouth of the D'Agro catchment, eastern Sicily. (b) Cumulative distribution function for grain size for a range of values of the fractal dimension. The cumulative distribution function that best fits the D'Agro data is shown (m = 0.27, D_f = 2.73). There is a greater contribution from fine grain sizes with higher values of the fractal dimension. From Allen et al. (2015b) (fig.3) with permission of University of Chicago Press.

bedload sediment in the main channels of the Pagliara, Fiumedinisi and Agro catchments etched into a region of active uplift at 1−1.5 mm yr^{-1} in northeastern Sicily; (2) coarse sediment at the outlet points of catchments distributed along strike of topographic ranges in Sicily and Basilicata-Campania, southern Italy; and (3) weathering products (regolith) in catchments in southern Italy developed on a range of different rock types. Together, these data sets provide a good idea of the typical fractal dimensions of sediments and regolith stored in upland catchments prior to export to sedimentary basins.

Details of sample localities and the methods used to collect particle size data are given in Allen et al. (2015b). The fractal dimension can be calculated in two ways. First, taking the logarithm of both sides of equation (9.16) gives a straight line relationship between $M(X < x)/M_T$ and x/x_{max} if the distribution is fractal (Figure 9.9), where the slope is

https://doi.org/10.1017/9781316135754.010 Published online by Cambridge University Press

$m = 3 - D_f$ (equation (9.17)). Equation (9.16) has been used to determine the fractal dimension from sieve data collected at 19 localities at the outlets of Sicilian catchments. Second, the value of the fractal dimension at each station along the main channel of 3 catchments in Sicily was interpolated by taking the proportion by weight at two characteristic grain sizes, D_{84} and D_{50}, using a modification of equation (9.16):

$$m = \frac{\log P(X < D_{84}) - \log P(X < D_{50})}{\log(D_{84}) - \log(D_{50})} \tag{9.18}$$

where $P(D_{84})$ and $P(D_{50})$ are the proportions by weight smaller than the 84th and 50th percentiles respectively.

The estimated values of fractal dimension from weathering products can be compared with those for sediment at the outlets of catchments in the same region. Sediment at the outlets of 23 catchments along the Vallo di Diano and East Agri faults in Campania-Basilicata have an average fractal dimension of 2.42 using the interpolation method. This value reflects the mixed bedrock lithologies, and is very close to the average of the weathering products in the tectonically uplifting catchments, showing that weathering products are little modified during the process of sediment mobilisation before export to adjacent basins. In addition, the variation in fractal dimension at catchment outlets is small compared to the variation in the regolith caused by lithological controls. This suggests that although the average fractal dimension changes little from regolith to catchment outlet, the source materials undergo some homogenisation. It is expected that large catchments are more effective at homogenisation than small, but no relationship between fractal dimension and contributing drainage area is evident.

In summary, the fractal dimension of weathering products and sediment at catchment outlets in southern Italy are identical and are a good indicator of the grain-size mix of the sediment supply to sedimentary basins. Likewise, in Sicily, the fractal dimensions of sediment sampled at a number of stations along the main trunk channels of three catchments are indistinguishable from those calculated from sediment at catchment outlets (Allen et al., 2015b).

9.3.1 Simulations Using a Variable Grain-Size Mix in the Supply

Simulations are carried out using a physical sediment transport model in order to test the sensitivity of stratigraphic architectures to variations in the grain-size characteristics of the supply.

Although the fractal dimension has the advantage of describing the grain-size distribution of sediment in one number, fractal distributions do not have meaningful values of mean and standard deviation since they are scale invariant. The fractal power law, represented by equation (9.15), however, has the same form as the Pareto distribution, which is described by a shape parameter a representing the spread of the distribution and a scale parameter k representing the minimum grain size (Schroeder, 1991; Hastings and Sugihara, 1993; Vidondo et al., 1997). The unknown parameters of the Pareto distribution can be evaluated by interpolation between specified grain-size values. Here, interpolation is carried out using values of the 84th and 50th percentiles derived from the cumulative function distribution

of grain size based on Wolman-type clast counts. If the proportion of a sample that has particles below a grain size D_b is denoted by P_b, and the proportion of a sample that has particles below a grain size D_c is denoted by P_c, the estimate of the shape parameter a is

$$a = \frac{\log(1 - P_b) - \log(1 - P_c)}{\log(D_c) - \log(D_b)} \tag{9.19}$$

and the estimate of the scale parameter k_P is given by

$$k_P = \left\{ \frac{P_c - P_b}{(1/D_b^a) - (1/D_c^a)} \right\}^{1/a} \tag{9.20}$$

Plots of fractal dimension D_f derived from sieved and clast count data versus Pareto shape parameter a derived from interpolation of D_{84} and D_{50} have a regression $D_f = 3 - 0.45a$. Making use of equation (9.17), it can be seen that $a \approx 2.22m$ (Figure 9.10).

The mean of the Pareto distribution μ_P is given by

$$\mu_P = \frac{ak_P}{a - 1} \tag{9.21}$$

for $a > 1$. This mean value for a Pareto distribution with a shape parameter a and scale parameter k_P can be used to calibrate the input to a sediment dispersal model. For the sediment samples analysed, μ_P ranges between approximately 10 and 60 mm.

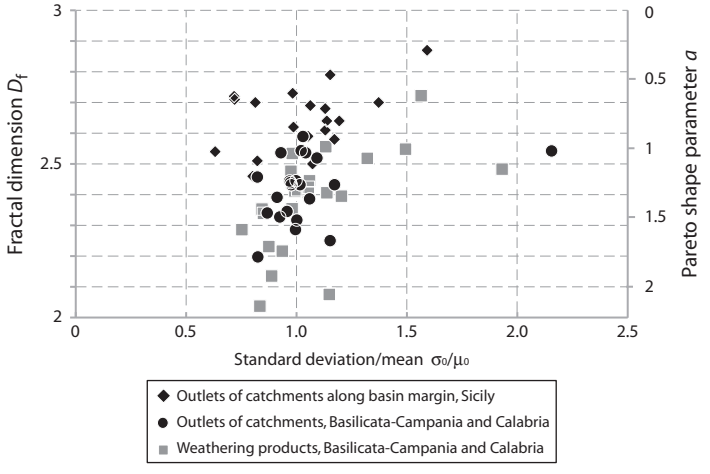

Figure 9.10 Plot of fractal dimension D_f and Pareto shape parameter a versus the ratio of σ_0/μ_0, for a range of sediments and regolith in the erosional engine. There are considerable uncertainties in associating fractal dimensions to particular values of σ_0/μ_0. The ratio σ_0/μ_0 is, however, centred on a value of about 1 and most values fall within the range 0.6–1.7. This range is incorporated in the simulations using a physical sediment transport model. After Allen et al. (2015b)(fig.8) with permission of University of Chicago Press.

https://doi.org/10.1017/9781316135754.010 Published online by Cambridge University Press

Sediment is initially dispersed down-system using a simple Sternberg-type exponential function of the form

$$\mu(x^*) = \mu_0 \exp(-Cy^*) \tag{9.22}$$

where μ_0 is the mean grain size of the sediment supply, taken as the mean of clasts with a Pareto size distribution μ_P, $\mu(x^*)$ is the mean grain size as a function of the normalised down-system distance $x^* = x/L$, L is the total depositional length of interest in the sediment routing system, $y^*(x^*)$ is the cumulative down-system sediment deposition in the normalised (mass balance) coordinate system, and C is a coefficient that describes the rate of decrease in mean grain size in the down-system direction. If the initial mean grain size is 60 mm, and the normalised cumulative down-system deposition is 0.5 (that is, half of the total sediment has been deposited), the mean grain size of the deposit ranges from 36 to 47 mm for values of C between 1 and 0.5 respectively. C therefore reflects the fractionation of clasts from the surface flux, which depends on its variance of grain size. This in turn should be inversely dependent on the Pareto shape parameter of the sediment supply. C is taken to be 0.75 in the simulations. The value of μ_P is used as the mean of the sediment supply μ_0 in equation (9.22), which becomes

$$\mu(x^*) = \frac{ak_P}{a-1} \exp(-Cy^*) \tag{9.23}$$

Equation (9.22) is a simplified version of that proposed by Fedele and Paola (2007) and applied by Duller et al. (2010) and Armitage et al. (2011), described in Section 9.4.3, which includes terms for variance of the grain-size distribution.

A plot of σ_0/μ_0 (where σ_0 is the standard deviation in the sediment supply and μ_0 is the mean grain size in the supply) using clast count data from catchment outlets along the topographic range front in Sicily and Campania-Basilicata, and from weathering products in Campania-Basilicata and Calabria, versus fractal dimension and Pareto shape parameter is shown in Figure 9.10. As D_f increases and a decreases, there is an increasing contribution to the distribution from small fragments, which is reflected in an increase in the value of σ_0/μ_0. Most values of σ_0/μ_0 fall in the range $0.6 - 1.7$, which corresponds to the range of $2 < D_f < 3$ and $0 < a < 2.22$ found in the southern Italian and Sicilian data sets. This range of σ_0/μ_0 is employed in the numerical simulations.

Simulations of the downstream fining of mean grain size are carried out with background subsidence approximated by an exponential function, analogous to an extensional half graben bounded by a border fault or to a flexural foreland basin (Allen and Allen, 2013). The discharge of the sediment supply and the spatial distribution of tectonic subsidence are kept steady during model runs. The surface processes model (Armitage et al., 2013) calculates sediment transport using the formulation of Smith and Bretherton (1972) with values of coefficients derived from Simpson and Schlunegger (2003). The boundary conditions are of fixed elevation at the downstream limit of the system at 10 km and at the head of the system there is a constant unit width supply of sediment of 1 m^2 yr^{-1} required to fill the basin.

https://doi.org/10.1017/9781316135754.010 Published online by Cambridge University Press

Two sets of simulations are carried out.

1. Set A: A simple exponential decline in mean grain size is combined with the physical sediment transport model with step-like (A1) and gradual (A2) changes in the starting mean grain size $\mu_P = \mu_0$ (Figure 9.11).
2. Set B: Sediment deposition is governed by the self-similar solution of equation (9.33) combined with the physical sediment transport model with step-like (B1) and gradual (B2) changes in the ratio of the standard deviation to the mean grain size in the sediment supply σ_0/μ_0 (Figure 9.12). C_v is held constant at 1.2 in the simulations and σ_0/μ_0 values are derived from field clast count data.

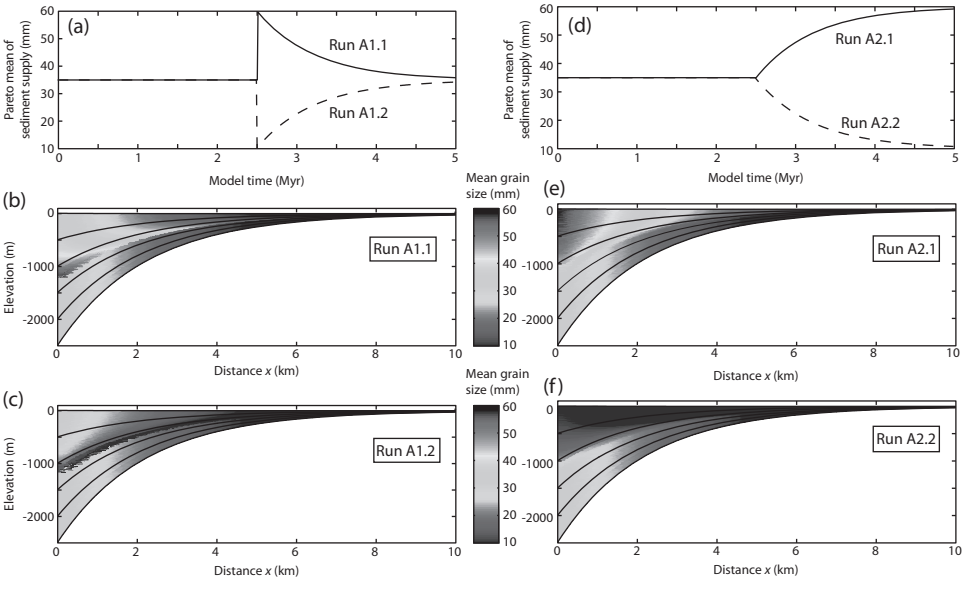

Figure 9.11 Simulation of grain-size variation over a 5 Myr time period in a half-graben or flexural-type basin with a maximum tectonic subsidence of 5 mm yr^{-1} using a Sternberg-type exponential decline in mean grain size. Four scenarios are modelled involving a step change increase (Run A1.1) and step change decrease (Run A1.2), and gradual increase (Run A2.1) and gradual decrease (Run A2.2) in the mean grain size of the sediment supply (μ_0), which has a distribution following the Pareto model. Step change and start of gradual change take place at 2.5 Myr. (b)-(c) and (e)-(f) show cross-sections of the basin with stratigraphy grey coded for mean grain size $\mu(x)$. (b) shows the effects of a step change increase in μ_0 from 35 to 60 mm, which causes an abrupt upward coarsening and an advance of the gravel front, followed by retrogradation. (c) shows the effects of a step change reduction in μ_0 from 35 to 10 mm, which causes an abrupt upward fining in grain size and upstream retraction of the gravel front, followed by gradual progradation. (e) shows the effects of a gradual increase in μ_0 from 35 to 60 mm, which causes an upward coarsening and prolonged progradation leading to a down-system extension of the gravel front. (f) shows the effects of a gradual reduction in μ_0 from 35 to 10 mm, which causes an abrupt upward fining in grain size and upstream retraction of the gravel front. From Allen et al. (2015b)(figs.9, 10) with permission of University of Chicago Press.

https://doi.org/10.1017/9781316135754.010 Published online by Cambridge University Press

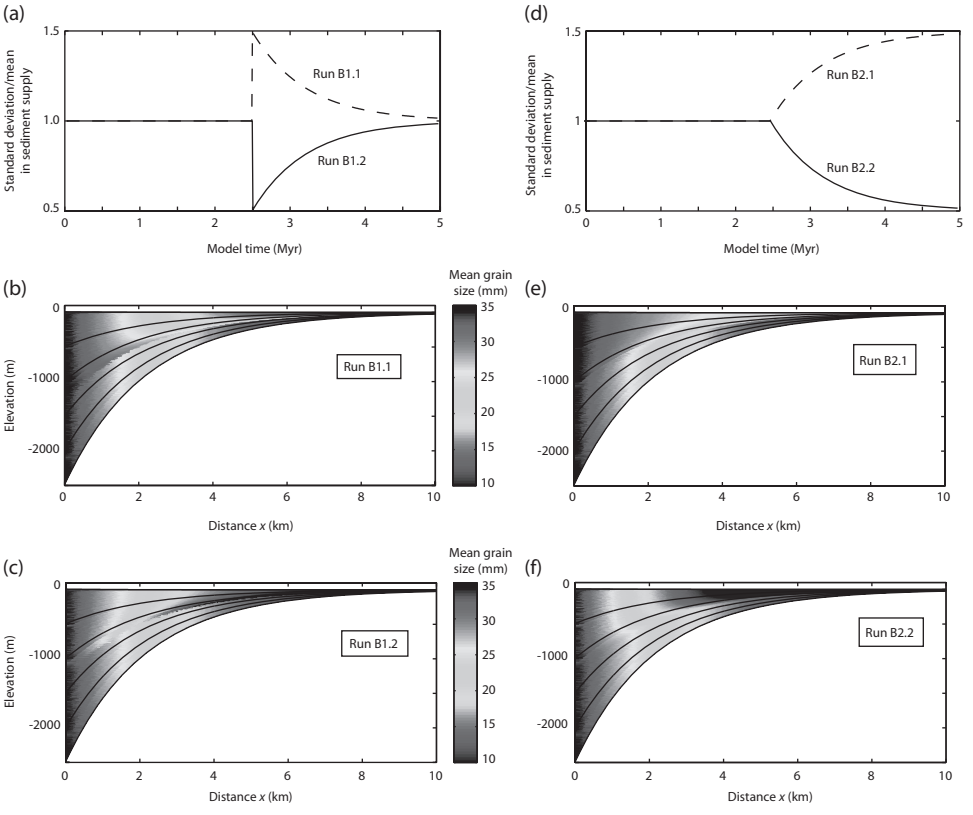

Figure 9.12 Simulation of grain-size variation in a half-graben or flexural type basin with a maximum tectonic subsidence of 5 mm yr^{-1} over a 5 Myr time period using the self-similar solution of Fedele and Paola (2007). Four scenarios are modelled involving a step change increase (Run B1.1), step change decrease (Run B1.2), gradual increase (Run B2.1) and gradual decrease (Run B2.2) in the ratio σ_0/μ_0 at 2.5 Myr. (b)-(c) and (e)-(f) show cross-sections of the basin with stratigraphy grey coded for mean grain size $\mu(x)$. (b) shows the effects of a step change increase in σ_0/μ_0 from 1 to 1.5, which causes an abrupt upward coarsening in grain size and a downstream extension of the gravel front. (c) shows the effects of a step change reduction in σ_0/μ_0 from 1.0 to 0.5, which causes an abrupt upward fining in grain size and a retreat of the gravel front, followed by slow progradation. (e) shows the effects of a gradual increase in σ_0/μ_0, which causes an upward coarsening in grain size and progressive down-system extension of the gravel front. (f) shows the effects of a gradual reduction in σ_0/μ_0, which causes a slight upward fining of mean grain size and minor retrogradation. From Allen et al. (2015b)(figs.11, 12) with permission of University of Chicago Press.

In the case of the simple exponential model, the Pareto mean grain size in the sediment supply is held constant at 35 mm before a step or gradual change at 2.5 Myr model time. The step change involves a doubling or halving of the Pareto mean followed by 2.5 Myr of relaxation. In the case of a gradual change, the Pareto mean increases or decreases to values of 60 mm and 10 mm after 5 Myr model time. In the simulations using the self-similar

https://doi.org/10.1017/9781316135754.010 Published online by Cambridge University Press

solution of Fedele and Paola (2007), the value of σ_0/μ_0 is set at 1.0 for the first 2.5 Myr, then increases to 1.5 or decreases to 0.5 in step or gradual changes. It is emphasised that the patterns of grain size in basin stratigraphy shown in the simulations are entirely driven by variations in the statistical properties of the grain-size mix of the sediment supply.

Simulations using the simple exponential model show marked shifts in grain size at the time of the step change. A step-like increase in the mean size of the sediment supply causes an abrupt upward coarsening and the down-system extension of the gravel front, followed by gradual retrogradation, producing a tongue or sheet of coarse gravel. A step-like decrease in mean grain size of the supply causes an abrupt upward fining and retraction of the gravel front. A gradual increase in the mean size of the supply causes an upward coarsening, but the trend is relatively slow and leads to long-term progradation. Likewise, the gradual reduction in the mean size of the supply results in a basin-wide fining in stratigraphy and long-term retrogradation.

Sedimentary architectures generated in simulations using the self-similar solution are consistent with those using the simple exponential model. A step-like increase in the ratio σ_0/μ_0 results in a pronounced gravel tongue, whereas the step-like descrease produces a surface marked by strong but short-lived retrogradation. A gradual increase in the ratio σ_0/μ_0 causes an increase in progradation, resulting in a long-term trend of upward coarsening. A gradual decrease causes long-term retrogradation and slow upward fining.

9.4 Grain-Size Fractionation in Sediment Routing Systems

9.4.1 Downstream Changes in Hydraulic Geometry

The downstream fining of grain size in river channels is accompanied by changes in the hydraulic geometry of the channels. Parker (1978b) suggested that gravel bed rivers configured themselves so that the shear stress on the bed at the centre of the channel is in excess of the critical stress required to entrain the median grain size. That is,

$$\frac{\tau_0}{\tau_{c\,50}} = \epsilon \tag{9.24}$$

This excess stress factor ϵ has been estimated at $1.2 - 1.8$ (meaning $20 - 80\%$ excess) in gravel reaches (Figure 9.13). Beyond the gravel front, however, the excess stress factor increases markedly to greater than 10, accompanied by an abrupt decrease in D_{50} and slope. By invoking the resistance equation for steady flow down an inclined plane and assuming that $\tau_{c\,50} \propto D_{50}$, equation (9.24) can be modified to

$$\epsilon = \frac{\rho g R S}{0.045(\rho_s - \rho) g D_{50}} \tag{9.25}$$

or

$$k = \frac{RS}{D_{50}} \tag{9.26}$$

https://doi.org/10.1017/9781316135754.010 Published online by Cambridge University Press

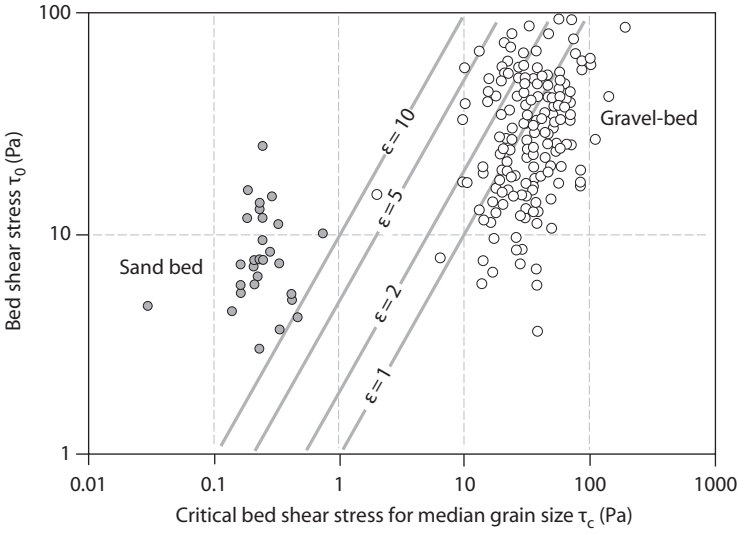

Figure 9.13 Excess shear stress relationship for 235 gravel bed and sand bed rivers for bankfull conditions, using data from Church and Rood (1983). The critical shear stress on the bed for the median grain size is assumed to be proportional to D_{50}. Modified from Robinson and Slingerland (1998)(fig.3) with permission of Society of Economic Paleontologists and Mineralogists.

where R is the hydraulic radius and k contains all the constants. That is, a downstream fining in the median grain size D_{50} only occurs where the product RS decreases downstream. Downstream variation in the hydraulic radius may be complex, particularly as a result of changes in channel width. Robinson and Slingerland (1998) compared a number of regime equations in terms of their success in predicting the variation in ϵ and channel width W across the gravel front. The best fit with observational data for 70 Canadian rivers was with

$$W = 3.83 Q_w^{0.528} D_{50}^{-0.07} \tag{9.27}$$

following Bray (1982), where the coefficient is likely to vary from approximately 1 to 4.5 depending on vegetation. A value of ~2 is thought appropriate for rivers with cohesive, vegetated banks. In equation (9.27), a reduction of grain size causes flow width to increase, and an increase in discharge of water also causes the flow width to increase. For example, if the water discharge is 100 $m^3\ s^{-1}$ and the median grain size is 0.02 m in the gravel reach, channel width $W = 57$m. In the sand reach, if the median grain size decreases to 0.0005 m and the water discharge does not change, the river nearly doubles its width to $W = 107$ m.

9.4.2 Fractionation of Grain Size During Dispersal

It is not clear what changes take place in the grain-size distribution of sediment as it is mobilised from regolith, transported and sorted by hydraulic processes and eventually

https://doi.org/10.1017/9781316135754.010 Published online by Cambridge University Press

selectively extracted from the surface flux and transfered to the substrate. These various processes are likely to have a multiplicative effect (Dacey and Krumbein, 1979).

McEwen, Fessenden, and Rogers (1959) suggested that processes associated with transport such as abrasion and fracturing caused the grain-size distribution to be modified, stating that (p.492)

> The cumulative effect of the various agents and processes acting on the sediment after its formation will, in general, impose a log-normal size distribution on the sediment.

If this were the case, it would be in agreement with the long-held view that the size distribution of transported sediments is commonly log-normal (Krumbein, 1938).

Allen et al. (2016) compared exponential (Rosin and Weibull 'laws'), Pareto and log-normal statistical models in fitting grain-size data collected from a range of sediment types involving different amounts of transport. Although these unimodal statistical models do not allow for mixing of end-member size distributions (Weltje and Prins, 2003), systematic variations in the goodness-of-fit of models to observed gravel-grade sediment size distributions allow the impact of mobilisation and transport to be assessed.

Sediment types were sampled from the regolith and bedload sediment of trunk channels in catchments serving as source regions (southern Italy and Sicily), proximal debris flow deposits that have suffered little granulometric change during emplacement (Owens Valley, California), and fluvial gravels that have been transported far from source (Eocene-lower Oligocene Escanilla and Antist systems of the southern Pyrenees of northern Spain and Miocene-Pliocene of the Great Plains, United States) (Figure 9.14).

The closeness of the cumulative distribution functions of the Pareto, Weibull and log-normal models to the observed cumulative function distribution of field data can be evaluated quantitatively using the Kolmogorov–Smirnov vertical difference parameter D_{KS}. This parameter is the greatest deviation of a cumulative distribution function of grain-size data from a reference or model cumulative distribution. Consequently, small values of D_{KS} indicate a close fit.

Ibbeken (1983) found that although jointed and weathered bedrock in southern Calabria, Italy, had a Rosin (Weibull) distribution, gravelly sediments sampled near the mouths of rivers where they enter the Ionian Sea, up to 20 km distant, were commonly bimodal with a sand fraction that was log-normally distributed. The log-normal property of sands is most likely imparted by transport processes causing hydraulic sorting (Middleton, 1976). A comparison of the goodness of fit of sediment in the erosional engine, at catchment outlets and as far-field fluvial gravel shows that the Rosin (Weibull) distribution is the poorest fit, particularly in far-field gravels (Figure 9.15). The log-normal distribution and the truncated Pareto distribution improve in the closeness of their fit with field data with increasing mobilisation and transport. This suggests that increasing fluvial transport enhances the log-normality of clast size distributions, as suggested by Krumbein (1938) and McEwen, Fessenden, and Rogers (1959).

Although fragment sizes in sedimentary materials from regolith to far-field gravel have a broad log-normality, increasing down-system, the Pareto model, base truncated to account

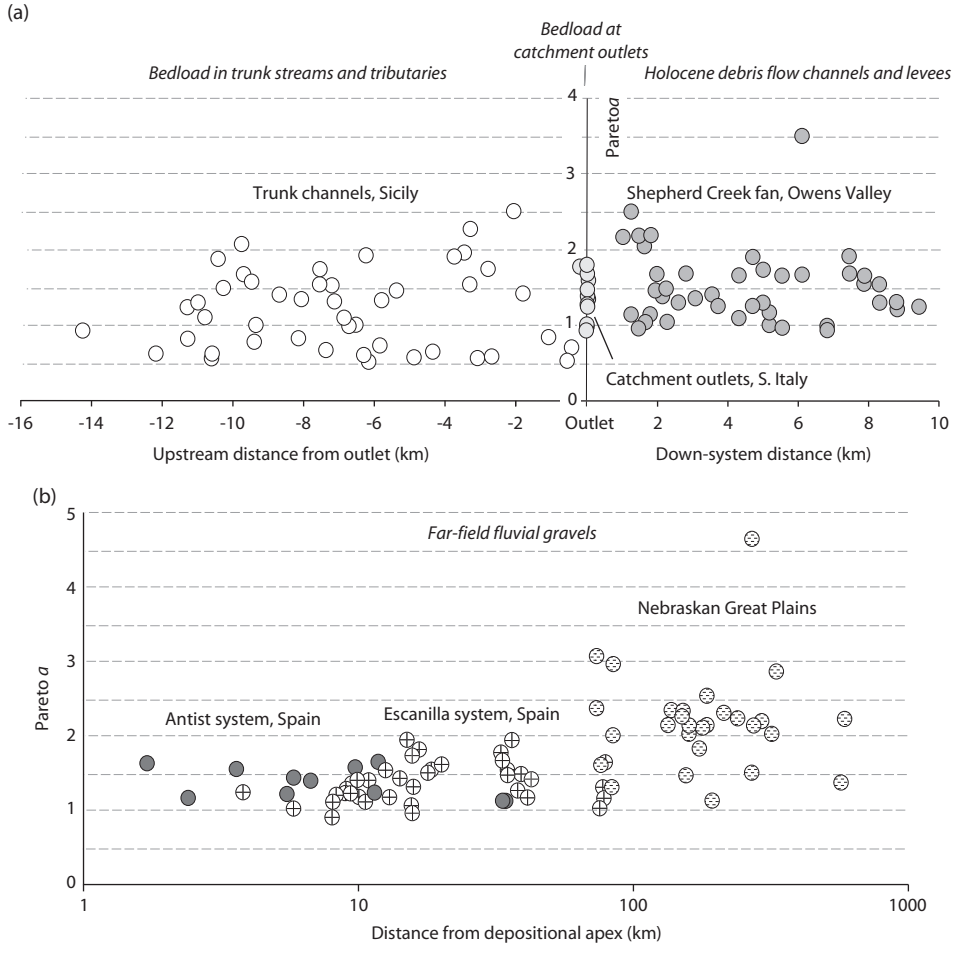

Figure 9.14 Compilation of estimates of the Pareto shape parameter *a* as a function of down-system distance. (a), Regolith, bedload in trunk channels and at catchment outlets, and proximal debris flow deposits. (b), Fluvial gravels, shown with a logarithmic scale for the down-system distance from the depositional apex. The average value of Pareto *a* increases with down-system distance, most likely driven by the loss of coarse particles by selective deposition. After Allen et al. (2016) (fig.26) with permission of John Wiley & Sons Inc.

for the finite minimum grain size (scale parameter k_P), also provides a good fit with the coarser half of the clast size distribution of field data from source to sink, and has the advantage of having a shape parameter that is potentially diagnostic of sediment transport and depositional processes. This shape parameter is well constrained in the erosional engine. On release into sediment transport systems, the clast size distribution may evolve predictably, moderated by the role of selective deposition. At short transport distances, shown by the Escanilla system, rapid deposition in proximal positions causes the extraction

https://doi.org/10.1017/9781316135754.010 Published online by Cambridge University Press

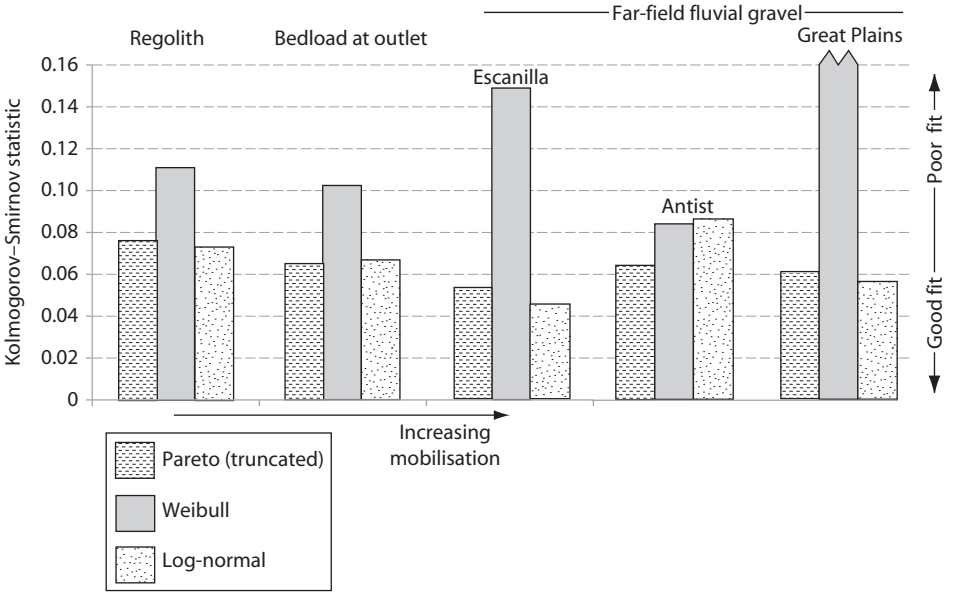

Figure 9.15 Kolmogorov–Smirnov goodness of fit statistic D_{KS} for weathering products (regolith in Basilicata, Campania and Calabria, southern Italy), coarse bedload in channels at catchment outlets (Pagiliara, Fiumedinisi and Agro catchments, Sicily) and far-field fluvial gravels (Escanilla palaeo-sediment routing system, south-central Pyrenees and Miocene-Pliocene of the Great Plains, United States). Whereas the Weibull model shows a worsening fit with degree of sediment mobilisation, the truncated Pareto and log-normal models show an improving fit with increasing mobilisation. Note that the Pareto statistics refer to the coarser half of the clast size distribution. After Allen et al. (2016)(fig.27) with permission of John Wiley & Sons Inc.

of the coarsest grains into stratigraphy, causing the shape parameter a to decrease from the value associated with the sediment supply from the erosional engine (Figure 9.16). At longer transport distances, or at positions further down-system in terms of the total mass balance (Martin et al., 2009; Michael et al., 2013), shown by the Great Plains system, the clast size distribution is enriched in relatively small particles compared to the sediment supply because of up-system selective deposition combined with abrasion during transport, increasing the shape parameter a (Figure 9.14). Consequently the Pareto shape parameter can potentially be used as an indication of proximality.

Despite the large down-system changes in mean grain size and gravel percentage from source region to depositional sink, particle size distributions appear to maintain log-normality over a wide range of transport distance. Consequently, full grain-size distributions can be predicted within the terrestrial segment of sediment routing systems given simple laws of downstream fining. These full grain-size distributions may help to inform the estimation of hydraulic properties of aquifers and oil and gas reservoirs, such as porosity and permeability. Use of statistical models therefore enables down-system fractionation of sediment released from source regions to be better understood and predicted and is a potentially valuable tool in source-to-sink approaches to basin analysis.

https://doi.org/10.1017/9781316135754.010 Published online by Cambridge University Press

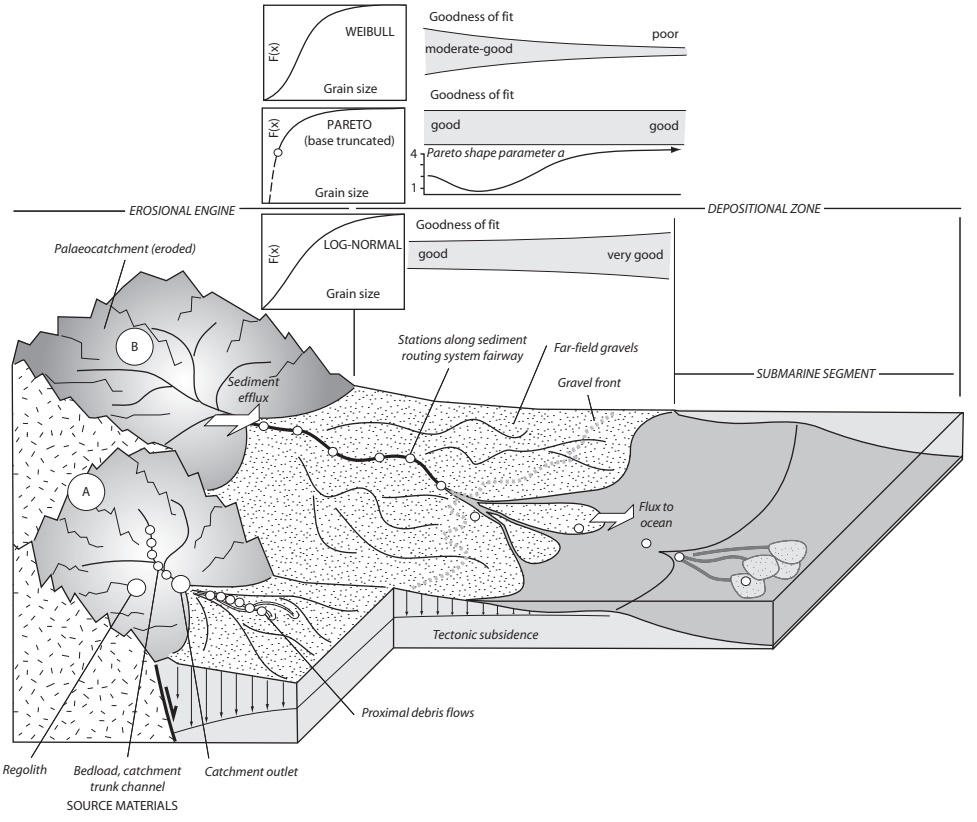

Figure 9.16 Schematic sediment routing systems showing the context of the samples analysed. A, Small coarse grained catchment-fan system with samples collected from regolith, channel bedload and sediment at the catchment outlet, which are indistinguishable from proximal debris flows in terms of Pareto shape parameter *a*. B, Large palaeo-sediment routing system with a catchment not preserved in the geological record. Stations are distributed along the sediment routing system fairway in the down-system direction. The truncated Pareto, Weibull and log-normal models are shown as cumulative distribution functions and in terms of goodness of fit, evaluated using the Kolmogorov–Smirnov statistic . The down-system variation of the Pareto shape parameter *a* is based on a compilation of all data sets and is partly speculative. After Allen et al. (2016)(fig.28), with permission of John Wiley & Sons Inc.

9.4.3 Down-System Fining of Gravel by Selective Deposition

In the absence of tributary inputs of sediment, grain size fines downstream in river systems. Basin-wide grain-size trends may be controlled by the relative mobility of mass, whereby the less mobile clasts are extracted first by a process of selective deposition. In many sedimentary systems, the observed rate of fining is too rapid to be explained by abrasion alone (Attal and Lavé, 2009) and consequently selective deposition must dominate. Field-based, numerical and laboratory studies (Toro-Escobar et al., 1996; Seal et al., 1997;

https://doi.org/10.1017/9781316135754.010 Published online by Cambridge University Press

Sheets et al., 2002; Fedele and Paola, 2007; Paola et al., 2009; Duller et al., 2010; Armitage et al., 2011; Whittaker et al., 2011; Paola and Martin, 2012; Parsons et al., 2012; Rohais et al., 2012) have focused on understanding and decoding regional grain-size trends in this context.

Over many repeated sediment transport events, a portion of the mobile sediment flux is extracted to build stratigraphy. Stratigraphy is therefore a strongly filtered record of this succession of sediment transport events. The selective extraction of mass from the mobile sediment flux during downstream transport produces a characteristic trend in preserved grain size. This grain-size trend in turn affects fluvial style and depositional environments (Strong et al. 2005). Critical to the prediction of downstream fining (Fedele and Paola, 2007; Duller et al., 2010; Whittaker et al., 2011; Allen and Heller, 2012) is the influence of the spatial distribution of tectonic subsidence $\sigma(x)$ on the downstream trend in the long-term sediment transport rate $q_s(x)$ (Figure 9.17). This downstream trend in $q_s(x)$ reflects the interplay between the volumetric discharge of the sediment supply and the volume extracted to fill accommodation.

The impact of deposition is to reduce the sediment discharge q_s in the downstream direction from its initial value $q_s(0)$ at x=0. Eventually, the sediment supply is exhausted at a depositional length L_d. At each point in the downstream direction $x < L_d$ the solid sediment volume extracted by deposition as a fraction of the surface sediment flux is $(1 - \phi)\sigma(x)/q_s(x)$, where ϕ is the porosity of the deposited sediment. The mean grain size of the deposited stratigraphy therefore depends on the grain-size characteristics in the supply and the downstream extraction controlled by the spatial distribution of deposition. Consequently, granulometric trends are potentially valuable in constraining parameters describing the volumetric budget of sediment routing systems (Whittaker et al., 2011; Parsons et al., 2012).

Since both $q_s(x)$ and $\sigma(x)$ are determined by the tectonics and climate of the basin and its hinterlands, different basin types are expected to contain sediment routing systems with characteristic rates of downstream fining. For example, it is possible to discriminate between catchment-fan systems filling small wedge-top basins in thrust belts, which have rapid rates of downstream fining, from large, coalesced fluvial systems spreading sediment from the cores of mountains belts to distant foredeeps, which have low rates of downstream fining (Duller et al., 2010; Whittaker et al., 2011; Allen et al., 2013).

Allowing for the porosity (ϕ) of deposited sediment, and defining the depositional length L_d as the point at which the sediment discharge is exhausted, the downstream variation of the sediment discharge can be written

$$q_s(x) = q_s(0) - (1 - \phi) \int_0^{L_d} \sigma(x)\mathrm{d}x \tag{9.28}$$

The sediment discharge can be calculated for different analytical expressions of the accommodation, or the model initialised with field observations. As an example, if the accommodation is given by an exponential model, decreasing away from the source region with a decay constant a, so that $\sigma(x) = \sigma_{max}\exp(-ax)$, equation (9.28) becomes

https://doi.org/10.1017/9781316135754.010 Published online by Cambridge University Press

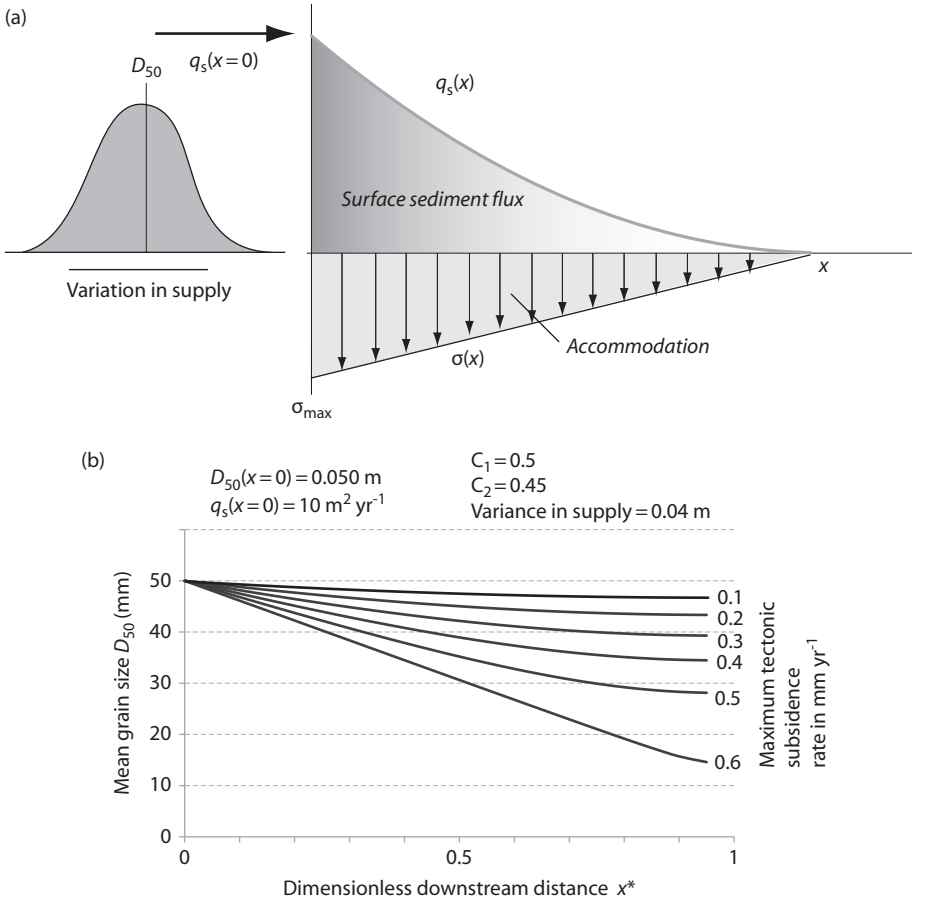

Figure 9.17 Downstream fining model with linear tilting for tectonic subsidence, showing downstream reduction of surface sediment flux q_s in (a). Mean grain size is shown for different values of maximum tectonic subsidence rate in (b).

$$q_s(x) = q_s(0) - (1-\phi)\left[\frac{\sigma_{max}}{a}\exp(-ax) + 1\right] \tag{9.29}$$

Alternatively, for a sinusoidal distribution of accommodation, with a wavelength λ, increasing from zero at $x = 0$ to a maximum σ_{max} at $x = \lambda/4$, equation (9.28) becomes

$$q_s(x) = q_s(0) - (1-\phi)\left[\sigma_{max}\frac{-\lambda}{2\pi}\cos\left(\frac{2\pi x}{\lambda}\right) - 1\right] \tag{9.30}$$

Equation (9.28) can easily be adapted to consider the sediment discharge for gravel only:

$$q_g(0) = f_g q_s(0) \tag{9.31}$$

https://doi.org/10.1017/9781316135754.010 Published online by Cambridge University Press

for $x < L_g$, where f_g is the gravel fraction in the supply and L_g is the distance to the gravel front. Since at each point in the downstream direction $x < L_g$ the solid sediment volume extracted by deposition as a fraction of the surface sediment flux is $(1 - \phi)\sigma(x)/q_s(x)$, the non-dimensional parameter for the extraction from the surface flux by deposition R becomes

$$R(x) = (1 - \phi)L_g \frac{\sigma(x)}{q_s(x)} \tag{9.32}$$

by introducing the length term L_g in the numerator.

The x-axis can be transformed by setting $x^* = x/L_g$, in which case the integration of $R(x)$ over the normalised downstream distance x^* gives the cumulative downstream sediment deposition in relation to the available surface flux, $y^*(x^*)$. The dimensionless parameter $y^*(x^*)$ can be used to calculate the variation of mean grain size $D(x)$ from an initial mean grain size D_0 and variation ψ_0 in the sediment supply (at $x = 0$),

$$D(x) = D_0 + \psi_0 \frac{C_2}{C_1}\left[\exp(-C_1 y^*) - 1\right] \tag{9.33}$$

where C_1 and C_2 are constants related to the variation in the grain-size distribution (Fedele and Paola, 2007; Duller et al., 2010; Whittaker et al., 2011). C_1 is 0.5 and C_1/C_2 is 0.70 in the application in Duller et al. (2010).

The grain-size trend therefore reflects the grain-size distribution of the sediment supply, the sediment discharge from the upstream source, and the spatial distribution of accommodation (Duller et al., 2010; Parsons et al., 2012) (Figure 9.18). The rate of down-system fining decreases with increasing sediment supply, as indexed by increasing states of basin filling, F. F is a dimensionless parameter representing the ratio of q_{s0} to accommodation creation due to tectonic subsidence:

$$F = \frac{q_{s0}}{\int_0^{L_d} \sigma(x)\mathrm{d}x} \tag{9.34}$$

so that the basin is underfilled when $F < 1$ and overfilled, leading to sediment bypassing the model basin at $F > 1$ (Figure 9.18).

9.4.4 Effects of Climate Change on Grain-Size Trends

In the rivers of the High Plains of the United States (Figure 9.19), which drain the Rocky Mountains, channel slopes have decreased since the Miocene (McMillan, Angevine, and Heller, 2002), suggesting that they have responded to climatic mechanisms rather than tectonic (see Wobus, Tucker, and Anderson (2010) for a discussion of the differentiation of climatic and tectonic forcing on river long profiles). There is a twofold increase in median grain size of sediment exported from the Rocky Mountains across the Miocene-Pliocene boundary (Duller et al., 2012) (Figure 9.20). This twofold increase is attributed to climatic

https://doi.org/10.1017/9781316135754.010 Published online by Cambridge University Press

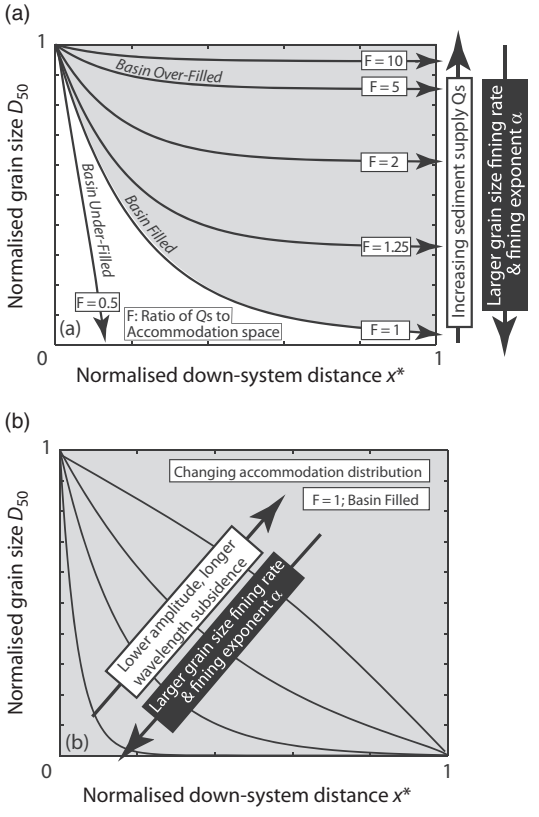

Figure 9.18 Down-system fining of grain size for different values of sediment supply (a) and tectonic subsidence (b). Perfect filling of the basin is at $F = 1$. Increased sediment supply leads to lower rates of downstream fining. For a filled basin, down-system fining is more rapid when the spatially exponential subsidence is higher amplitude and lower wavelength. After Duller et al. (2010) (fig.2) with permission of American Geophysical Union.

warming in the Pliocene, when there was higher precipitation and greater seasonality. River slopes $S(x)$ can be estimated from a Shields stress inversion of median grain size D_{50}

$$S(x) = \frac{1.4\tau_c^* \Delta\rho D_{50}}{H} \tag{9.35}$$

where τ_c^* is the critical Shields stress for entrainment of sediment on the river bed (0.05), H is channel depth and $\Delta\rho$ is the excess sediment density ($\rho_s - \rho_w$). Slope can be found by assuming that local shear stresses on the bed are 1.4 times the critical shear stress (Paola and Mohrig, 1996). Equation (9.35) can be combined with a resistance equation to derive estimates of unit width water dsicharge q_w (Figure 9.20b). D_{50} and H are constrained from field observations. The doubling of median grain size of the supply between the Miocene and Pliocene is associated with an increase in water discharge from $1-3$ m^2 s^{-1} to $3-6$ m^2 s^{-1}, and the thick succession of Pliocene Broadwater sediments suggest aggradation on the Great Plains after 3.7 Ma, consistent with high rates of sediment supply.

https://doi.org/10.1017/9781316135754.010 Published online by Cambridge University Press

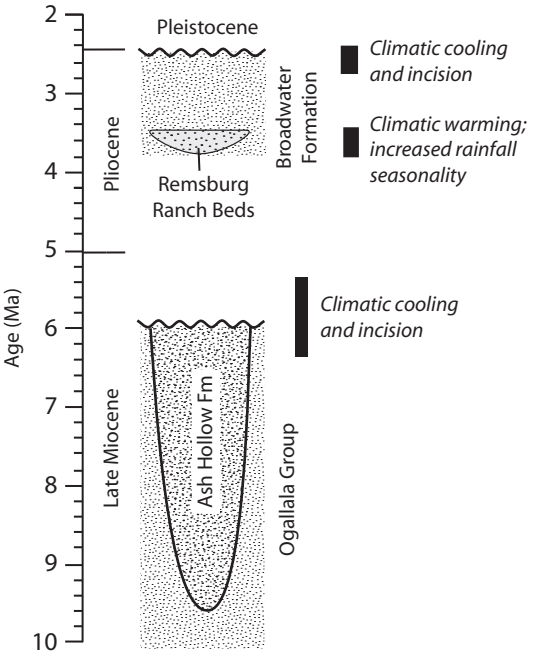

Figure 9.19 Fluvial stratigraphy of the Nebraskan High Plains from 10 Ma to the present day. Modified from Duller et al. (2012)(fig.1) with permission of Geological Society of America.

In numerical models where erosion has the form of a diffusive-concentrative equation (Smith and Bretherton, 1972; Simpson and Schlunegger, 2003) including a term for tectonic uplift, precipitation was doubled and halved (from a steady-state value of 1 m yr^{-1}) in order to investigate the effect of climate change on the grain-size distribution and stratal geometries in the basin (Whittaker et al., 2011). Doubling of the mean annual precipitation generated a sharp increase in sediment flux before returning to a steady-state value with a response time of about 0.5 Myr. The increased sediment flux causes a lengthening of the fan and an increase in median grain size. A halving of the precipitation rate causes a sharp reduction in sediment flux that returns to the steady-state value with a response time of approximately 1 Myr. The reduced sediment flux causes an abrupt backstepping of the fan toe and shrinkage of the fan. This backstepping is accompanied by an increase in the rate of down-system grain-size fining.

An increase in precipitation will increase the sediment grain size exported from the catchment because channel bed grain size scales on bed shear stress. The coupling between an increase in precipitation and an increase in sediment calibre leads to the marked progradation down-system of a gravel sheet with a duration of the order of the response time. The deposition of conglomeratic sheets down-system has previously been linked to increases in precipitation in the upstream catchment (Heller and Paola, 1992).

https://doi.org/10.1017/9781316135754.010 Published online by Cambridge University Press

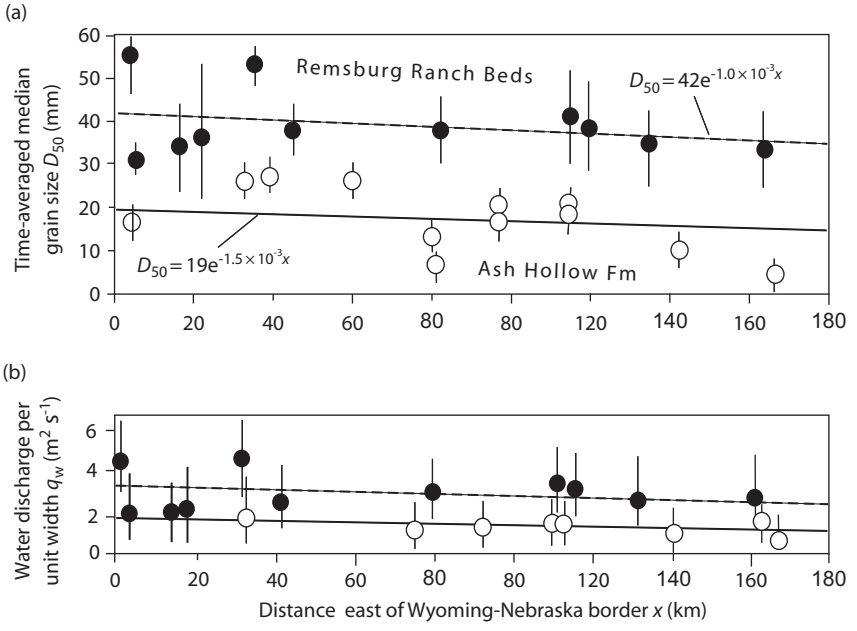

Figure 9.20 (a) Time-averaged median grain size of the upper Miocene Ash Hollow Formation and lower Pliocene Remsburg Ranch Beds. Grain sizes derived from Wolman point measurements ($n =$ 80 for RRB and $n = 45$ for AHF). Vertical bars are the error associated with the combined median grain-size value. (b) Water discharge per unit width q_w predicted from measurements of median grain size and slope. Grain sizes and calculated water discharges are higher for the Pliocene Remsburg Ranch Beds than for the upper Miocene Ash Hollow Formation. From Duller et al. (2012) (figs.2, 4) with permission of Geological Society of America.

The Palaeocene-Eocene boundary (55 Ma) in the Tremp Basin of the Spanish Pyrenees coincides with the presence of the Claret conglomerate sheet (Figure 9.21). The Claret Conglomerate is about 1 – 4 m-thick (locally up to 8 m) and bounded above and below by different paleosols that indicate an increase in precipitation rate over time (Schmitz and Pujalte, 2007). Climates and environments changed from semi-arid alluvial plains with small channels to a vast conglomeratic braidplain under a much wetter climate regime. The Claret Conglomerate is an extensive sheet with an erosive, low-relief base, covering an area of at least 500 km^2. However, the source of the conglomerate lay approximately 10 km to the northeast of the most proximal outcrops, so the braidplain may have covered an area of 2,000 km^2 at the Palaeocene-Eocene boundary. Maximum clast size is 65 mm, much coarser than pebbles in underlying channels, which rarely exceed 25 mm. The braidplain formed over a short time period of a few thousand years (~10 ky) directly after the Palaeocene-Eocene boundary. Such a short-lived pulse is consistent with the timescale of a transient response to a climatic perturbation in the model runs of Armitage et al. (2011).

The Palaeocene-Eocene thermal maximum (PETM) is registered in the marine time-equivalent stratigraphy of the Pyrenean Gulf in the form of a 2–4 m-thick (locally

https://doi.org/10.1017/9781316135754.010 Published online by Cambridge University Press

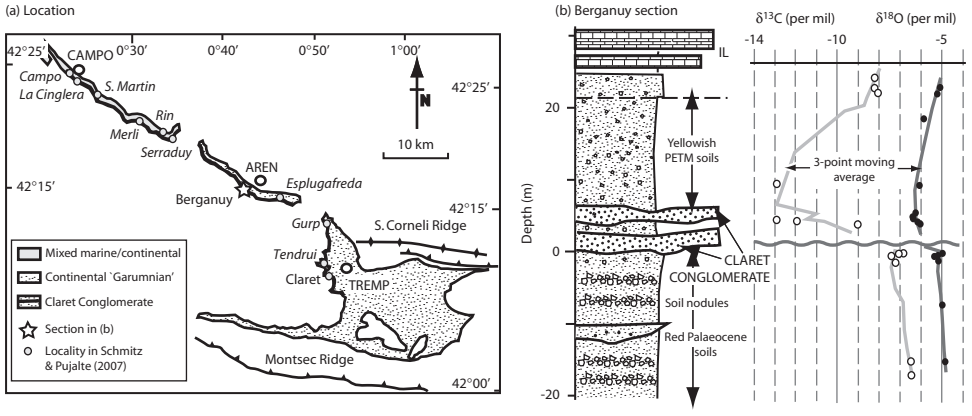

Figure 9.21 (a) Location of Claret Conglomerate at the Palaeocene-Eocene boundary in south-central Pyrenees. The Tremp Basin was an alluvial plain that passed westwards into a carbonate platform. (b) The stratigraphic section at Berganuy, showing isotopic data from carbonate nodules. Red paleosols with relatively positive carbon and oxygen isotopes are found in the Palaeocene, which pass up via the Claret Conglomerate into yellowish isotopically light paleosols of the Palaeocene-Eocene Thermal Maximum (PETM). IL refers to carbonates of the Ilerdian transgression. Modified from Schmitz and Pujalte (2007) (figs.1, 3) with permission of Geological Society of America.

up to 20 m) unit of clays intercalated within a carbonate-dominated succession (Pujalte, Baceta, and Schmitz, 2015). The clays represent a massive input of terrestrial siliciclastic sediment into the ocean attributable to the profound hydrological changes associated with the PETM. In addition, coarse-grained siliciclastics infilled incised valleys and a long-lived deep marine channel. The presence of coarse and fine-grained terrestrial siliciclastics in the Pyrenean Gulf coeval with the development of an extensive fluvial braidplain illustrates the down-system propagation of the climate signal through the sediment routing system.

9.5 Linking Source to Sink: Provenance Tools

The English poet William Blake wrote in 'Auguries of Innocence' (written 1803, published 1863):

To see a world in a grain of sand
And a heaven in a wild flower,
Hold infinity in the palm of your hand,
And eternity in an hour.

'Auguries of Innocence' contains a number of paradoxes where innocence stands alongside evil and corruption. An augury is a sign or omen. I doubt that Blake was thinking of provenance when he wrote those lines, but I do think he was marvelling at the big picture contained in small things, together with the contradictions and tensions. It seems improbable at first sight that global climate changes and tectonic movements might be

https://doi.org/10.1017/9781316135754.010 Published online by Cambridge University Press

reflected in the properties of a grain of sand. 'To see a world' of vanished source areas from a 'grain of sand' is an example of an inverse approach in the study of provenance. Provenance studies using the inversion of multiple proxies are a powerful way of linking sources to sinks, but do not capture the transformations that take place during weathering and transport. To develop models of such transformations, both compositional and textural, requires forward modelling calibrated by targeted field observations.

The chief inverse method of linking source to sink is to match the petrography, mineralogy, or chemistry of detrital grains to a source region using specific tracers. For many years a range of techniques has been applied to the study of the provenance of sand-grade sediment, including analysis of light fraction petrography (Zuffa, 1985) and heavy minerals (Mange and Maurer, 1992; Mange and Wright, 2007). Bulk and single-mineral geochemistry, isotopes and thermochronometers are increasingly used to constrain both the location and rock type of source areas and their exhumation history. U-Pb geochronology of detrital zircons allows the ages of eroding parent rocks to be identified and provides valuable insights into provenance.

The crystallisation age of zircons can be measured using the U-Pb decay series, usually with laser ablation ICP mass spectrometry. The distribution of U-Pb crystallisation ages can be compared with cooling ages obtained from fission track analysis of detrital and bedrock zircon samples. Double-dating allows zircon ages representing slow cooling during exhumation to be discriminated from ages representing rapid crystallisation due to volcanic or plutonic activity (Garver et al., 2000). Using U-Pb ages of detrital zircons to identify source regions and understand sediment trajectories is now a very well established and standard provenance tool. It is commonly used in conjunction with an analysis of heavy minerals, clast compositions and light fraction petrography (as an example, see Nicholson et al. (2014)).

Data sets containing U-Pb ages, heavy mineral point counts and petrographic point counts need to be extensive in order to be statistically meaningful. Consequently, statistical techniques are employed to quantify the pairwise distance between sample attributes that are fed into a multidimensional scaling (MDS) algorithm (Vermeesch, 2013). MDS visualises data as a map that preserves the difference between samples as relative distances between data points. An example is the analysis of sand samples from the Taklamakan desert to discriminate between a northerly provenance by wind and a southerly and westerly provenance by flowing water (Rittner et al., 2016). Consideration of heavy mineral, petrographic and U-Pb geochronological data collected from river bed and aeolian dune sands in the Taklamakan desert and from possible source areas surrounding the Tarim Basin (Figure 9.22) allowed the authors to conclude that the bulk of the sand originates from rivers draining the mountains in the southeast (Altun Shan), south (Kunlun Shan) and west (Pamir), but not by winds blowing predominantly from the Junggar Basin and Altai in the north.

Bulk petrography is analysed by point counting, using quartz, feldspar and lithic fragments as the main grain types. Lithic fragments are commonly subdivided into volcanic, sedimentary and metamorphic varieties. Mineralogy is conventionally illuminated from

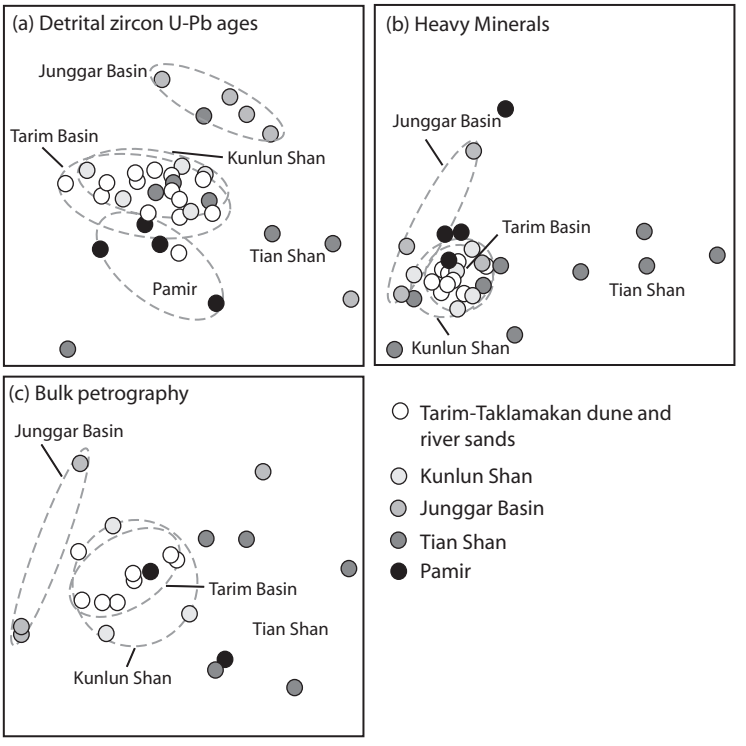

Figure 9.22 Multidimensional scaling maps of detrital zirocn U-Pb ages, heavy mineral assemblages and light-fraction petrography for modern river and aeolian dune sands. Tarim Basin sands form a distinct cluster that is overlapped by a field for the tributaries of the Kunlun range. Samples from rivers draining the Karakorum and Pamir form a cluster adjacent to the Kunlun and Tarim data. Samples from the Junggar Basin fall well outside the Tarim Basin cluster. Samples from the Tian Shan do not form a coherent cluster due to their heterogeneity and possibility of reworking. Modified from Rittner et al. (2016) (supplementary material fig.1) with permission of Elsevier.

ternary plots of heavy minerals: for example, pyroxene+olivine; the ultrastable group of zircon, tourmaline and rutile+garnet; and amphibole+the metamorphic trio andalusite, kyanite and sillimanite. Nicholson et al. (2014) used an apatite-tourmaline index ATi and a garnet-zircon index GZi to compare modern sands with older stratigraphy.

The sand in the Taklamakan desert can also be compared with the aeolian dust comprising the Chinese Loess Plateau and with other desert regions of NE China such as the Mu Us and Tengger deserts, and with the sediment load of the Yellow River (Figure 9.23). The Yellow River shows the closest affinity to loess sediments, as well as to the Mu Us desert, but there is no evidence to suggest that the Taklamakan desert is the source of dust for the Chinese Loess Plateau.

Drawing a linkage between sediment in the depositional sink and source regions can be carried out using other geochemical fingerprints. Weathering and sediment transport

https://doi.org/10.1017/9781316135754.010 Published online by Cambridge University Press

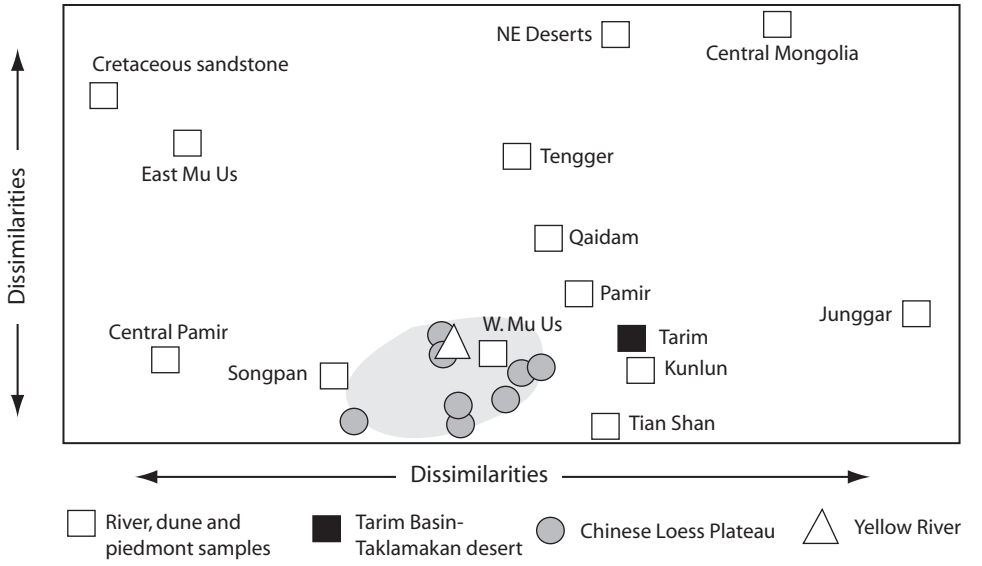

Figure 9.23 Multidimensional scale (MDS) map based on calculated Kolmogorov–Smirnov distances between U-Pb age spectra. Tarim Basin sands are compared with a range of possible source areas, modern sediment samples from the Chinese Loess Plateau and data from the upper reaches of the Yellow River. Modified from Rittner et al. (2016) (fig.5) with permission of Elsevier.

processes are not expected to result in isotopic fractionation, so the measured isotopic signature of any given sediment should reflect the bulk composition of the source. For example, $^{143}Nd/^{144}Nd$ isotopic values in clays recovered from the Bengal Fan are similar to those of modern sediments in the Ganga River (Goldstein, O'Nions, and Hamilton, 1984) and Bengal Fan sediments have been linked to denudation of source regions in the Himalaya (Bouquillon et al., 1990).

Eocene sedimentary rocks from the Gulf of Tonkin are uniformly less negative in ϵ_{Nd} than modern Red River sediment, indicating that Eocene sediments are more radiogenic and have younger crustal sources than the modern Red River. The Eocene samples are closer, however, to the ϵ_{Nd} of Tibetan sources for the Upper Yangtze River. Pb isotope analysis of single grains of feldspar allows further discrimination of the basement sources for the Eocene of the Gulf of Tonkin and supports the existence of Tibetan sources, but the differences with the modern Red River samples suggests that the Gulf of Tonkin received Yangtze Block detritus from the Middle Yangtze River before drainage capture by the Red River at some stage after the Eocene (Clift, Layne, and Blusztajn, 1994). A similar approach (Pb and Nd) was taken to the sediments of the River Indus (Clift et al., 2001b, 2002), supplemented by analysis of garnet geochemistry (Alizai, Clift, and Still, 2016). Provenance tools are therefore capable of highlighting major river drainage reorganisation events in contributing source areas.

https://doi.org/10.1017/9781316135754.010 Published online by Cambridge University Press

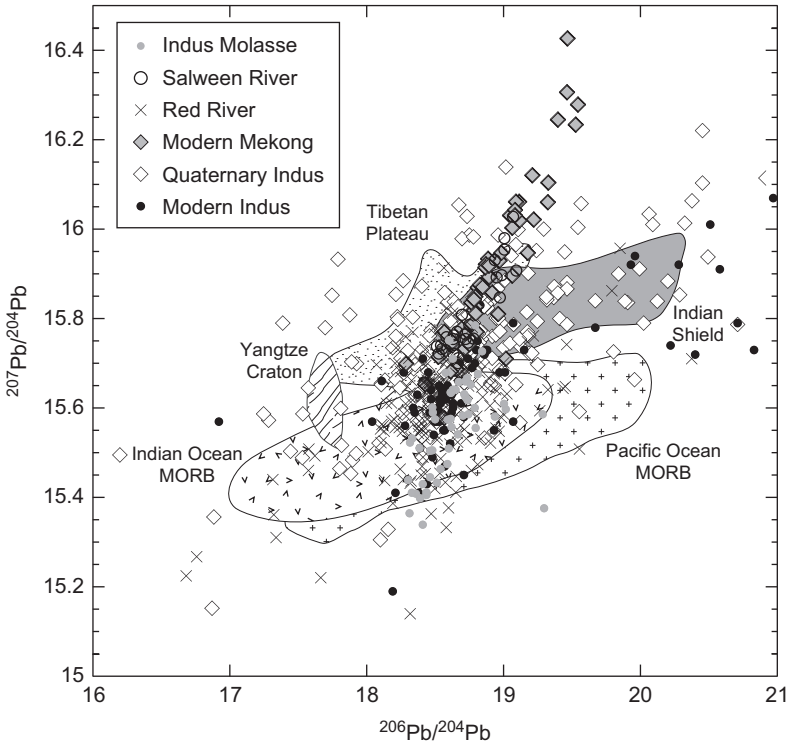

Figure 9.24 Lead isotope cross-plot of a number of detrital samples from modern rivers, Quaternary deposits and Neogene Molasse stratigraphy compared to possible source terranes. MORB; Mid-Ocean Ridge Basalt. Detrital grains plotting within the MORB fields are likely eroded from primitive arc-type sources within oceanic suture zones. Note that each set of sediments spans both primitive and more evolved continental sources, indicating a mixed provenance. Because the possible basement source rocks are not comprehensively surveyed many grains fall outside the defined fields (in this case the Yangtze Craton, Tibetan Plateau and Indian Shield). Grains with higher isotope ratios, especially $^{207}Pb/^{204}Pb$ tend to represent erosion of ancient continental crustal blocks. Data sources: Indus Molasse (Clift et al., 2001b); modern Indus River (Clift et al., 2002); Quaternary Indus River valley (Alizai et al., 2011); Red River (Clift et al., 2008b); Salween and Mekong Rivers (Bodet and Schärer, 2000); Indian and Pacific MORB (Stracke, Bizimis, and Salters, 2003). From Peter Clift (pers. comm.).

Lead isotopic ratios measured in detrital K-feldspars can be used to compare modern deposits from their ancient equivalents and correlatives (Figure 9.24). Modern sands and Quaternary and Neogene detrital equivalents are widely spread in a plot of $^{207}Pb/^{204}$ versus $^{206}Pb/^{204}$, indicating mixing from more than one source. MORB, Indian continental crust, Yangtze craton and Tibetan Plateau occupy partly overlapping fields in terms of their Pb isotope characteristics.

https://doi.org/10.1017/9781316135754.010 Published online by Cambridge University Press